Flapping Wing Flight Dynamic Modeling

Benjamin Y. Leonard

Thesis submitted to the Faculty of the

Virginia Polytechnic Institute and State University

in partial fulfillment of the requirements for the degree of

Masters of Science

in

Aerospace Engineering

Mayuresh J. Patil, Chair

Craig Woolsey

Richard D. Snyder

August 22, 2011

Blacksburg, Virginia

Keywords: Flight Dynamics, Flapping Flight

Report Documentation Page		*Form Approved* *OMB No. 0704-0188*

1. REPORT DATE **22 AUG 2011**	2. REPORT TYPE	3. DATES COVERED **00-00-2011 to 00-00-2011**
4. TITLE AND SUBTITLE **Flapping Wing Flight Dynamic Modeling**		5a. CONTRACT NUMBER
		5b. GRANT NUMBER
		5c. PROGRAM ELEMENT NUMBER
6. AUTHOR(S)		5d. PROJECT NUMBER
		5e. TASK NUMBER
		5f. WORK UNIT NUMBER
7. PERFORMING ORGANIZATION NAME(S) AND ADDRESS(ES) **Virginia Polytechnic Institute and State University,Blacksburg,VA,24061-0002**		8. PERFORMING ORGANIZATION REPORT NUMBER
9. SPONSORING/MONITORING AGENCY NAME(S) AND ADDRESS(ES)		10. SPONSOR/MONITOR'S ACRONYM(S)
		11. SPONSOR/MONITOR'S REPORT NUMBER(S)

12. DISTRIBUTION/AVAILABILITY STATEMENT
Approved for public release; distribution unlimited

13. SUPPLEMENTARY NOTES

14. ABSTRACT
Highly agile, hover capable apping wing ight is a relatively new area of study in engi- neering. Researchers are looking to apping ight as a potential source for the next gener- ation of reconnaissance and surveillance vehicles. These systems involve highly complicated physics surrounding the apping wing motion and unusual characteristics due to a hover re- quirement not normally associated with conventional aircraft. To that end this study focuses on examining the various models and physical parameters that are considered in various other studies. The importance of these models is considered through their e ect on the trim and stability of the overall system. The equations of motion are modeled through a quasi co- ordinate Lagrangian scheme while the aerodynamic forces are calculated using quasi-steady potential ow aerodynamics. Trim solutions are calculated using periodic shooting for sev- eral di erent conditions including hover, climb, and forward ight. The stability of the trim is calculated and examined using stroke-averaged and Floquet theory. In ow and viscous ef- fects are added and their e ects on trim and stability examined. The e ects of varying hinge location and the inclusion of stroke deviation in the wing kinematics are also explored. The stroke-averaged system was not found to be a direct replacement for the periodic system as the stability was di erent for the two systems. In ow and viscosity were found to have large e ects on the stability of the system and models accounting for the two should be included in future ight dynamic models.

15. SUBJECT TERMS

16. SECURITY CLASSIFICATION OF:			17. LIMITATION OF ABSTRACT	18. NUMBER OF PAGES	19a. NAME OF RESPONSIBLE PERSON
a. REPORT **unclassified**	b. ABSTRACT **unclassified**	c. THIS PAGE **unclassified**	**Same as Report (SAR)**	**107**	

Flapping Wing Flight Dynamic Modeling

Benjamin Y. Leonard

(ABSTRACT)

Highly agile, hover capable flapping wing flight is a relatively new area of study in engineering. Researchers are looking to flapping flight as a potential source for the next generation of reconnaissance and surveillance vehicles. These systems involve highly complicated physics surrounding the flapping wing motion and unusual characteristics due to a hover requirement not normally associated with conventional aircraft. To that end this study focuses on examining the various models and physical parameters that are considered in various other studies. The importance of these models is considered through their effect on the trim and stability of the overall system. The equations of motion are modeled through a quasi coordinate Lagrangian scheme while the aerodynamic forces are calculated using quasi-steady potential flow aerodynamics. Trim solutions are calculated using periodic shooting for several different conditions including hover, climb, and forward flight. The stability of the trim is calculated and examined using stroke-averaged and Floquet theory. Inflow and viscous effects are added and their effects on trim and stability examined. The effects of varying hinge location and the inclusion of stroke deviation in the wing kinematics are also explored. The stroke-averaged system was not found to be a direct replacement for the periodic system as the stability was different for the two systems. Inflow and viscosity were found to have large effects on the stability of the system and models accounting for the two should be included in future flight dynamic models.

Acknowledgments

I would like to thank Dr. Patil and Dr. Woolsey for giving me the opportunity to work on my thesis here at Virginia Tech. I appreciate you providing me an interesting topic to work on and always being there to help me with understanding difficult topics and with communicating my ideas to others.

I'd also like to thank Dr. Snyder and everyone at AFRL for providing funding and help on this project. I also appreciate all of the feedback and support I received from Dr. Kapania and the rest of the CCMS here at Virginia Tech.

To my parents, I don't think I can thank you enough for all you've done for me over the years. Your constant support and encouragement, not to mention trips to help me move and always having a place for me to visit on holidays has made everything I've done easier and much more enjoyable. I'll go ahead and thank my sister here too since she has always been available for help moving and moral support (even though she's younger and really should thank me for all the wisdom I've bestowed).

My roommates over the years: Mike, Corey, Max, Will, and Karen thanks for tolerating my complaining and helping me remember to have fun too. I especially owe you one, Will and Karen, for taking me in when I would have been a homeless grad student.

To my office mates (at one time or another) Eric, Jeff, Will, Chris, and Max, thanks for making my work a little more fun. I particularly enjoyed the trips downtown, weekly lunches, and harassment for being the Masters/youngest student in the office (Jeff I'm still expecting a second thesis sometime in the next ten years).

Contents

List of Figures

ix

List of Tables

Chapter 1

Introduction

1.1 Motivation

The Defense Advanced Research Project Agency (DARPA) defines a Micro Air Vehicle (MAV) as an aircraft limited in all of its dimensions to 15 cm [4]. This size limitation is meant to allow the vehicle to operate in a confined space such as those presented by an urban canyon or building interior. While any type of aircraft could theoretically be adapted to fit the MAV definition, rotor craft and flapping wing designs are particularly well adapted for the high agility and maneverability requirements of this difficult operating environment. Further more, for concealment in plain sight, flapping wing designs are particularly well-suited in that they can mimic designs we see in nature and thereby have the potential to hide in plain sight. Of particular interest in demonstrating these capabilities are recent developments in highly agile, hover capable, flapping-wing aircraft that mimic small fliers in nature such as Aerovironment's Nano Hummingbird [5].

This particular study focuses on the difficulty of determining what models are most important to consider when trying to accurately represent flapping wing dynamics. Consideration is given to eventual control synthesis and calcuation of dynamic metrics such as performance, stability, maneuverability, and gust response. To this end, various models such as viscous

forces and inflow, and physical parameters, such as deviation and hinge location are considered. These models are incorporated into an otherwise quasi-steady aerodynamic model (integrated over the span using blade element theory) which is coupled with a rigid-body quasi-coordinate Lagrangian scheme.

1.2 Literature Review

The literature review consists of three sections. The first deals with flight dynamics and equations of motion with an emphasis on those methods that have been applied to flapping wing systems. The second section deals with the various aerodynamic models that have been used on flapping wings. The third deals with stability and control.

1.2.1 Aerodynamics of Flapping Wing Systems

Fry et al. [6] examined the kinematics and aerodynamics of Drosophila flight, specifically rapid maneuvers, using high-speed infrared photography. The captured kinematics were played through a dynamically scaled robot in order to measure the produced aerodynamic forces. The maneuvers in question are described as saccades, fast turns that can involve as much as ninety degree turns in less than fifty micro seconds. Results showed that the mean forces generated by the fruit fly were fairly constant with respect to the body axes. Instead, during maneuvers, the body orientation was changed in order to facilitate overall acceleration (along with very slight changes in wing motion). The paper also examines the assumption that smaller animals must overcome primarily viscous friction forces while larger animals are dominated by inertial forces when accelerating or turning. Through analysis of the time course data for the torque produced by the insect, it was concluded that the very small fruit fly was not dominated by viscous friction forces but instead by inertial forces. It is also stated that while the research was conducted on the fruit fly, the results are relevant for nearly all insects in that inertial forces only become more important as size increases and

the turns observed were banked turns similar to those observed in larger insect species.

Continuing this work, in Fry [7] the body and wing kinematics of Drosophila flies were characterized through the use of high-speed video, lasers, and a dynamically scaled robot. The motion was captured using high-speed cameras focused on a 0.5 cm^3 area in a control volume lit by infrared LEDs (which are not visible to the flies and so do not disrupt their behavior). The robot was then used to 'replay' motions captured by the video and measure the aerodynamic forces caused by these motions. A U-shaped motion was observed in the wings of the hovering flies with no observed 'clap and fling' motion. Quasi-steady aerodynamics were found to be able to account for nearly all of the behavior involved in hovering except that there are discrepancies between measured and model data that indicate the presence of unsteady mechanisms. The paper also details the comparison between tethered and untethered flight of the flies and how the stroke pattern is severely disrupted by the tethering. This refutes the historical methods of using tethered flight as a proxy for hovering flight, instead showing that the tethering makes for different stroke patterns and a significant pitch down moment. Fry proposes that this is an effect of sensory disruption. They conclude by describing the balance necessary between flight forces for stable hovering and the challenge this produces with two high frequency wings. They propose that the complex nature of the still poorly understood hinge may hold the key to permitting a limited number of muscles to make the subtle changes in strokes necessary to control insect flight. A table providing the parameters and power numbers measured in the experiment is also provided as an important resource.

Singh and Chopra [8] examine the aerodynamics of insect-based, biomimetic, flapping wings in hover. A biomimetic flapping wing test mechanism was used to imitate insect wing flapping. The mechanism was a passive-pitch bi-stable mechanism controlled by a speed controller, pulse generator, and brushless motor. Due to vibration and inertial loads, mounting the apparatus on a load cell did not provide very meaningful results. Instead, load cells made of strain gages were mounted at the base of the wings to measure the moments caused by the wings. The motion of the wings (pitch angle) was measured using a Hall sensor

(a magnet moving past the Hall effect sensor causes a relative charge). Inertial loads were measured by running the mechanism in a vacuum chamber (90% vacuum). Low frequency tests were run for wings I-III and results reported for wings II and III. Wing I and II were of the same form (wing II had thicker Mylar) which was an aluminum frame around all edges of the frame and the wing surface itself made of Mylar. Wing III was similar but the frame did not continue around the trailing edge, but instead only around the leading edge and the root. High frequency results were reported for wing III, and several tests were also carried out for a series of lightweight wings that used carbon fiber frames rather than aluminum frames. Results were also given for several of these light wings. The analytical model for the forces accounted for translational and rotational circulation, the leading-edge vortex effects, noncirculatory forces based on thin airfoil theory, starting vortex effects, and shed wake and tip vortex effects. At low frequency wing III showed the most thrust (pitched about its 20% chord location) and showed more thrust at a pitch angle of 45 degrees rather than 30 degrees. When the frequency was increased to try and increase thrust the mass of the wing was shown to have a significant effect on the maximum possible frequency to which the mechanism could drive the wing. It was also noted that the thrust showed a sudden drop at a frequency of 11.6 Hz (wing III). All wings showed an eventual drop at high frequency, possibly due to a loss in noncirculatory thrust caused by elasticity. It was also noted that using a softer spring to control the passive pitching caused a larger pitch variation that resulted in a larger thrust at a smaller power consumption. Singh and Chopra propose that this passive mechanism merits further study due to its mechanical simplicity and ease of implementation.

Dickinson et al. [2] discuss the interaction of three interactive mechanisms that enhance aerodynamic performance. The three mechanisms are delayed stall, rotational circulation, and wake capture. Delayed stall occurs during the translational portions of the stroke while rotational circulation and wake capture occur during the stroke reversal. These rotational mechanisms can modulate the direction and magnitude of flight forces during steering maneuvers. When insect wings are placed in a wind tunnel and tested over the range of velocities normally encountered the measured forces are much lower than those required for

flight. They also discuss one of the first unsteady effects to be identified: clap and fling. This phenomenon precedes pronation and hastens the development of circulation during the downstroke. Clap and fling is not present in all insects and thus cannot be the solution to the lower than required forces presented in the wind tunnel tests. Delayed stall represents a flow structure on the leading edge of a wing that can generate circulatory forces greater than those experienced under steady-state conditions at high angles of attack. The 3D force coefficients are greater than those of the transient 2D steady-state values which confirm the presence of some transient unsteady effect such as delayed stall. Although the translational values with the delayed stall effects match the magnitude of the measured force near the middle of each half stroke they do not match the values during force reversal. A possible explanation for the peaks at the end of each half stroke could be a combination of rotational effects and wake capture. Rotational effects are similar to those effects experienced by a spinning baseball; air is pulled within the boundary layer and serves as a source of circulation. The wing must rotate to be in the proper position for each stroke. This rotation, however, can be altered to change the reaction forces caused by the rotational effects. If the wing flips early (before changing direction) then the resulting force should be upward. If the flip is late then the resulting force would be a downward force. If the flip spans both half strokes then the resulting downward and upward forces cancel. Therefore proper timing of wing rotation can add extra lift beyond that of just delayed stall. Delayed stall, however, does not account for the large positive transient that develops immediately after the wing changes direction. The researchers propose that wake capture is the other rotational effect that makes up the difference between the translational effects and the rotational effects. In wake capture the wing benefits from the shed vorticity of the previous stroke. The vorticity generated by the previous stroke increases the effective velocity of the next stroke and increases the force production. To support this hypothesis, the authors tested the force produced by halting the wing at the end of the half stroke. The results showed that wing generates force for several hundred milliseconds following the end of the half stroke. Again, the rotation timing has a similar effect to that of delayed stall. The authors conclude that the wing should rotate in

advance of the reversal so that it generates circulatory forces at the end of each stroke, and increases the strength of the wake and ensures proper orientation to take advantage of the wake. Insects alter this timing in order to aid in control. For instance the rotation timing on one wing can be altered to create more drag and aid in turning.

Zbikowski [9] discusses advances in fluid dynamics as applied to insects and micro air vehicles (MAVs). These new concepts are applied to two methods of aerodynamic modeling of an insect like wing in hover. One of the unsteady aerodynamic phenomena Zbikowski discusses is a spiraling leading-edge vortex. This vortex is bound, remaining on the wing during the half cycle throughout pitching, plunging, and sweeping before being shed at the end of the stroke when the wing flips. This is very similar to Dickinson's delayed stall effect. The other effects included those of wing pitching, plunging, and sweeping present at all times and wing interactions with its own wake (Dickinson's wake capture effect). The flow was assumed incompressible, low Reynolds number, and laminar with a rigid, thin wing of symmetric section. Zbikowski argues that these assumptions are well supported except for lack of flexibility in the wing which he adopts for simplicity. He proposes that insects deliberately force separation at the leading edge to gain vortical lift and shedding the vortex at the end of the half stroke using the sudden wing flip. The pitching, plunging, and sweeping nature of the wing are similar to aspects of helicopter blades but with the critical difference that MAV wings consistently flap with angles of attack greater than 20 degrees without having the vortex shed and losing lift. In insect like flapping the separation occurs at the beginning of the motion and generates stable lift (from the vortex) throughout the half cycle. The essence of Zbikowski's framework is to account for both the leading-edge vortex and the other part of the flow. The non-vortical part of the flow was treated with unsteady aerodynamics similar to those used in helicopter blades with attached flow, while the bound leading-edge vortex was considered a non-linear phenomenon and had to be treated with methods different from the thin airfoil theory. Using the circulation approach allows for the use of just a single framework since both the linear and nonlinear contributions can be handled consistently. Using the velocity potential necessitates using a second correction to deal with the nonlinear

components (in this case Polhamus's leading-edge suction analogy). The circulation approach uses a methodology based on linear, thin-airfoil theory applied to unsteady wing motions. The linear portions of the aerodynamics are handled with classical von Karman-Sears Theory and the nonlinear portions with McCune-Tavares nonlinear extensions. The velocity potential approach is based upon the theories of Theodorsen, Wagner, and Garrick supplemented by the Polhamus leading edge suction analogy. Zbikowski argues that the simplifications made in his paper are necessary now in order to further engineering design so that fundamental analyses will be furthered, leading to production of a better design.

Nagai et al. [10] detail experimental and numerical studies on the aerodynamic characteristics of an insect in forward flight (specifically the flapping wing). Much like in Dickinson's work, the unsteady aerodynamic forces and flow patterns were measured using a scaled mechanical model but in this case in a water tunnel instead of mineral oil. The wing and motions were based on the flapping wing of a bumblebee and the results were compared to a 3D Navier-Stokes code. The aerodynamic mechanisms of the wing, such as delayed stall, rotational effect, and wake capture, were examined in detail for forward flight. The motions played through the model were 'simple trapezoidal-type' motions based on data from Dudley and Ellington [11]. The mechanism was similar to that of Dickinson's in that the mechanism provided the three degrees of freedom and in the cases of forward flight the water was moved through the tunnel at 0.02 to 0.2 m/s. Because a bumblebee moves its hind and forewings together and not independently, the planform chosen for this wing encompassed both and was made of acrylic surrounded by an aluminum frame. Forces were measured at the root by strain gages in the typical fashion. For flow visualization the wing was slightly different in that it had no aluminum frame so that light could pass through the entire wing and it was made thicker to retain resistance to bending. Comparisons between the two wings showed 2% or less difference in aerodynamic characteristics. A laser shining through the side wall of the water tunnel was used as a light source and two cameras placed below the tunnel recorded the flow patterns. The three dimensional Navier-Stokes code has been validated by Isogai et al. [12, 13] in relation to the time histories (hovering flight) of aerodynamic forces for a

dragonfly. Three cases were chosen for validation in this experiment, a course grid, a fine grid, and a fine time-step case. All three cases were in good agreement with the experimental results. Flow patterns were also compared between the experimental and numerical results and again agreement between the two was good. There were small quantitative differences throughout the comparisons that were attributed to the differences in shape between the numerical and experimental wings. The experimental wing had a thickness as described previously with a rectangular leading edge while the numerical model had a sharp leading edge with zero thickness. This leads to a larger leading edge vortex in the experimental case than in the numerical one which may account for the difference in quantitative results.

Sane and Dickinson [14] compared instantaneous force measurements from a dynamically-scaled mechanical flapping wing to quasi-steady estimates in order to study rotational forces for a range of angular velocities and axes of rotation. It was found that the rotational coefficient varied as expected with axis of rotation but also varied with angular velocity (not expected based on theoretical models). The standard quasi-steady model was then modified to include rotational, translational, and added-mass effects. By subtracting this new quasi-steady estimate from the measured forces the aerodynamic effects due to wake capture were isolated. This paper also gives a brief description of what makes up each of the effects added to the standard quasi-steady estimate.

Peters et al. [15] extend classical thin airfoil theory by allowing for large frame motion of the wing and small deformations (expanded into Chebychev polynomials) relative to large frame motion (in particular for rotorcraft analysis). The theory itself is formulated in terms of the deflections and generalized forces within the frame and is based on transformations of the traditional potential flow equations. The equations are broken down into mass, damping and stiffness matrices, making coupling with finite elements or modal analysis convenient. Also the unsteady components of the aerodynamics are encompassed in a completely separate wake model making the theory flexible in that it can be changed to match the physics rather than relying on a constant unsteady model such as the flat wake found in Theodorsen's theory. This allows for a theory somewhere in between quasi-steady blade element theories

and CFD analyses in terms of accuracy and computation time. Peters et al. validated the theory against those of Theodorsen [16], Garrick [17], Loewy [18], Issacs [19, 20], Greenberg [21], Wagner [22], and von Karman [23] as well as experimental cases.

Pesavento and Wang [24] solved the two dimensional Navier-Stokes equations in relation to a piece of free falling paper at Reynolds number near 10^3. In contrast to an airfoil governed by the Kutta Joukowski condition which normally experiences lift proportional to velocity squared, the lift was found to be dominated by the product of the linear and angular velocities. In comparing the two models, the Joukowski model was modified to incorporate a lift-drag polar but this still did not exhibit the cusplike turning points with elevation of the center of mass. This difference was further investigated through decomposition of forces into added-mass and circulation terms and the Navier-Stokes equations are found to provide an extra instantaneous forcing term in the circulation due to the angular velocity.

Anderson et al. [25] continued the earlier work in [24], this time experimentally quantifying the trajectories of falling plates. The trajectories were captured using high-speed digital video in order to determine instantaneous accelerations from which to deduce the fluid forces. These values were compared to direct solutions of 2D Navier-Stokes equations. Again the fluid circulation was found to be dominated by a rotational term proportional to the angular velocity of the plate, unlike the lift typically found for an airfoil at an angle of attack. The torque was also found to be small in comparison to that normally found on an airfoil at a fixed angle of attack. By varying Reynolds number, dimensionless moment of inertia, and the thickness to width ratio of the plate, the dynamics varied from fluttering, tumbling, and chaotic motion. Variations in initial conditions provided a period of brief transients followed by periodic fluttering. These results matched well with the numerical results previously described in [24].

Berman and Wang [26]continued previous work done by Wang and others in [24, 25] by investigating aspects of hovering insect flight. Optimal wing kinematics that minimized power usage while constrained to provide enough lift for hover (maintain time-averaged constant altitude over a flapping period) were determined using a hybrid optimization that combines

aspects of genetic and gradient based optimizers. The wings examined in this study were considered as rigid bodies with three rotational degrees of freedom and are based on the wings of a fruit fly, bumblebee, and hawkmoth. In order to allow for the many cost function evaluations and detailed sensitivity analysis that go into the optimization procedure the quasi steady aerodynamics described in [24] were utilized. The results of the analysis provided kinematics which were qualitatively and quantitatively similar to observed data ([7, 27] among others). The data also showed a constant leading edge throughout the stroke (trailing edge never lead) being advantageous due to interactions between inertial and aerodynamic power.

Stanford et al. [3] examined the effects of several parameters on aeroelastic hovering motions of a flexible flapping wing. The parameters used in this study were wing shape, structural composition, and the kinematic motions, while the criteria for performance was the peak power required for the stroke subject to kinematic constraints. Because this work was completed at the partner organization Air Force Research Laboratory (AFRL) the aerodynamics of this study were of particular interest for comparison and validation. The aerodynamics consisted of a quasi-steady blade element model and a higher-order Navier Stokes flow solver (OVERFLOW-2.1). The quasi steady aerodynamics were based on those of Berman and Wang [26] and differ from those in this study due to the inclusion of viscous forcing terms as well as empirically determined forcing coefficients. With these terms included the quasi-steady aerodynamics were able to show good agreement with the CFD model despite the large difference in computational time and model fidelity.

Oppenheimer et al. [28] developed an aerodynamic model from blade element theory (not including unsteady effects) based on the work of Sane and Dickinson [14]. The vehicle considered in the work is similar to the Harvard RoboFly except that the wings are independently actuated using two different piezo electric actuators. The blade element theory is used to calculate instantaneous and stroke-averaged forcing and moments for use in control of the aircraft. The position of the wing is controlled using oscillators that change once per wing beat cycle so as not to invalidate the stroke-averaged model. A specific technique, Split-Cycle

Constant Period Frequency Modulation with Wing Bias, is introduced for tracking the wing motion that provides a high degree of control without actively controlling the angle of attack. Particularly the frequency of the wing upstroke and downstroke can be varied to generate a stroke averaged drag and a wing bias added to provide pitching moment control all while utilizing only a pair of actuators. Using the frequency modulation to control x and z forcing and the wing bias to control moments and y forcing two actuators can provide agile insect flight in untethered conditions.

1.2.2 Flight Dynamics of Flapping Wing Systems

Bierling [29] presents a flight dynamic model for flapping wing insects and/or MAVs. It assumes a rigid-body fuselage with wings that are attached at a single rotating joint (that move with a prescribed motion). The aerodynamic model used in his analysis is a quasi-steady model based on the work of Sane and Dickinson [30, 14]. A spline interpolation was used to approximate the observed data for the wing kinematics and this data was used to generate the final equations of motion (added to the nonlinear equations already derived from the Newton-Euler equations). A trim algorithm was used to calculate the periodic steady-state and Floquet analysis used to calculate flight dynamic modes and stability to small perturbation. The stability estimate from Floquet analysis were close to those from the stroke-averaged analysis except for slight differences in the lateral eigenvalues and the hovering case. This means that the quasi-steady approach may be used for simplification of the dynamics when necessary. In general the results pointed towards unstable or slightly unstable eigenvalues necessitating active control but also providing opportunities for high maneuverability. Bierling also concluded that the close agreement between the quasi-steady analysis and the Floquet results might be due to the low wing mass of the Drosophila model and that larger wing masses would create larger differences in the two analyses. The results neglect certain unsteady affects as part of the quasi-steady assumption and the results are only valid for the Drosophila wing with corresponding flapping frequency and Reynolds number.

Taylor et al. [31] examine the flight dynamics characteristics of a desert locust. The paper begins with a brief discussion of flapping flight dynamics in general and concludes that it is somewhat similar to forward rotary flight due to oscillatory mass and forcing. The authors discuss the distinction between open- and closed-loop dynamics as pertaining to insects. Insects in general have open-loop dynamics that are not easily separated from the flight mechanics. In general, blocking any kind of feedback usually results in a stop in flight. The authors go on to discuss the characteristics of the desert locust including its wings and its flight sensors. They also provide analogous aircraft sensors for many of the locust sensors, for example, the wind sensitive hairs on the head of the locust act as angle of attack sensors and side-slip vanes. The Oxford Zoology Department's low-speed closed-loop wind tunnel was used to measure flight dynamics parameters for three different desert locusts, while two others were measured in an open-throat blower tunnel. Linear time-invariant (LTI) and nonlinear time-periodic (NLTP) models for the flight dynamics were both analyzed. The models formulated by the authors predicted that locust flight would be unstable without visual feedback to the control system. The NLTP method was also discussed as a better solution than the LTI model due to the NTLP model's stronger forced oscillatory character. The authors also suggest that because the MAVs as dictated by DARPA will be on the same size order as the desert locust, a time-periodic modeling method will be necessary to capture their flight dynamics as well.

Meirovitch and Tuzcu [32] formulate the equations of motion for a flexible aircraft, integrating together dynamics, structural vibrations, aerodynamics, and controls. Of particular interest to this thesis was the formulation of the dynamic equations of the aircraft, treated as a multi-body system using quasi-coordinates. The motions of the body are broken into six degrees of freedom (based on the body axes attached to the undeformed fuselage) and combined with deformations of the flexible components. Further detail on the equations of motion in terms of quasi coordinates is provided in Meirovitch [33] and discussed later in this thesis.

Deng et al. [34] worked on mathematical modeling of flapping flight MAVs in the inch size

range. In this particular work they worked on the full system dynamic models, with particular emphasis on their differences with respect to traditional fixed and rotary wing MAVs. The particular models included the wing-thorax dynamics, aerodynamics (full flapping model at low Reynolds number), body dynamics, and a biomimetic sensing system. The mathematical models were derived from analytic solutions, empirical models, and biological data. These are integrated into algorithms for wing aerodynamics, body dynamics, actuator, dynamics, external environment, and flight control, which together make up the Virtual Insect Flight Simulator (VIFS). The aerodynamics are those of the Sane and Dickinson [14] though wake capture is neglected. The sensory system is novel in that it neglects traditional flight sensory techniques in favor of biomimetic sensors. Ocelli are used to estimate roll and pitch angle, while a magnetic compass estimates yaw. Halteres are used for angular velocity sensing and optic flow sensors (much like those described in Humbert et al. [35]) are used for navigation and to avoid impact. The reason given for these novel systems is that they would be lighter and draw less power than conventional systems, though currently they are only proposed and not actually in use.

Faruque and Humbert [36] developed a reduced order model for the longitudinal hovering dynamics of a fly-like insect. They utilized a quasi-steady aerodynamic model first utilized by Dickinson's group at Cal Tech (averaged for each period to a time invariant model) extended by perturbation states from hover (to help understand sensing and feedback requirements when moving away from stable flight) and rigid body equation of motion. They then used frequency based system identification to solve for the transfer functions from the control inputs to the states. The heave dynamics were found to be decoupled from the forward and pitch motions and use of the haltere system stabilized the vehicle which otherwise suffered from an unstable oscillatory mode (in agreement with previous CFD studies). This further reinforces the idea of passive stabilization mechanisms which help to reduce the computational requirements of these highly weight and power constrained vehicles.

Continuing work by Faruque and Humbert [37] examined the lateral motion about hover. The study continued to examine passive stability mechanisms and their implications for

flight control and stability. Using the previously described analysis, the lateral motion about hover was shown to have two stable poles and two lightly damped nearly unstable poles. One of the poles (stable) was uncoupled and corresponded to the yaw motion of the vehicle while the others were coupled roll/sideslip motions. Again the motions were found to have inherent passive damping mechanisms that help to stabilize the vehicle without control input. The designer can leverage these phenomena and reduce the burden placed on the vehicle computationally, reducing power, size, and weight issues.

Sun and Xiong [38] studied the longitudinal flight stability of hovering bumblebees using eigenvalue analysis to solve the equations of motion. The aerodynamic derivatives necessary for the analysis were computed using computational fluid dynamics (CFD). For longitudinally-disturbed motion they identified three natural modes though the instabilities arising from these modes were all such that the growing time was much greater than the wing-beat period and as such the bumblebee would have plenty of time to adjust wing motion. Sun and Xiong assumed the bee to be a rigid body (wings also inflexible) with six degrees of freedom and the flapping wings were simplified by calculating the wingbeat average forces and moments (per stroke). The inertia effects of the wings were also neglected (justified by calculating the wings' mass to be about 0.52% of the total insect mass). In this particular case, the equations of motion were linearized by approximating the body's motion as a series of small deviations from the reference condition (steady, symmetric flight). Sun and Xiong also state that near hover the body aerodynamic forces are minuscule as compared to those of the wings and therefore can be neglected without affecting the aerodynamic derivatives significantly. The eigenvalue analysis yielded one unstable oscillatory mode and two stable modes (subsistence modes). Sun and Xiong also explain the physical meaning of these motions and how the bee could easily overcome the instability that arises from the unstable mode.

1.2.3 Control of Flapping Wing Systems

Hamel and Jategaonkar [39] present a history of parameter identification in flight mechanics. It details the development of methods used in the past as well as currently. It also details the difficulties in determining aircraft parameters and how those difficulties have changed over the course of time. Some of the early methods presented were the first attempts as determining aerodynamic forces and included dynamic flight tests, the Longitudinal Oscillation Method, the Pulse Method of Dynamic Response Testing, the Time-Vector Method and Analog Matching. Most of these methods have become outdated, even at the time of the publication of this paper, and Hamel and Jategaonkar go on to present more modern methods of parameter estimation. Most of these methods were brought about with the advent and increase in power of computers, especially the personal computer. They also discuss four important aspects of parameter identification in modern methods, namely: design of the control input shape, selection of instrumentation and filters for high accuracy, definition of the structure/mathematical model, and proper selection of the time or frequency domain identification method. Each of these areas are discussed in depth and specific examples given. There is also a discussion on system identification applied to related topics. The paper goes on to conclude that the current techniques presented in the paper provided sufficiently accurate results and had been tested thoroughly enough to be considered powerful tools not only for research but also for industry. It also hypothesizes that the area of parameter identification will continue on limited only by the imagination and innovation of analysts, and motivated by the need to better understand aerodynamic phenomena.

Humbert et al. [35] deals with the nature of insect sensory feedback control and how it could be implemented in MAVs. The primary mechanism most desirable in insect sensory motor interaction is that of sensorimotor convergence. The output of sensory neurons is conducted directly to motor control centers rather than central processing areas for faster feedback than possible by first processing and then sending to motor centers. The visual sensory output focused on by this paper is optic flow, which is essentially the derivative of the objects in the optic field. The insect's eyes process the velocity of the objects in its optic field

and also their proximity. This minimized data is passed to the motor control centers for quick reactions and maneuvering. This is what gives insects their characteristic maneuverability and quick reaction times. Ideally, this data would also include the spatial structure and distribution of objects in the flow field to aid in navigation. Humbert et al. go on to describe the process of Wide-Field Integration (WFI) processing of ideal planar optic flow, including characterization and interpretation of WFI outputs. They also describe how output feedback of WFI sensory information can be used to create pitch altitude stability and terrain following capability (demonstrated using planar rotorcraft dynamics). It is concluded that terrain following applications to date have only utilized a small amount of the information available from optic flow. It would be possible to significantly improve terrain following, closed loop stability, and performance through proper implication of optic flow sensing. They demonstrate a methodology of stability through optical flow data with a minimum of sensory information from other methods. For instance only a measurement of forward speed was necessary to achieve zero steady state error in tracking altitude reference, and only pitch orientation necessary for hover equilibrium.

Hedrick et al. [40] discuss passive yaw stabilization in a wide range of flapping fliers. They propose that rather than actively damping out oscillations and perturbations, flying organisms use passive stability which damp out angular velocity through a methodology the authors term flapping counter torque (FCT). Their model predicts similar damping on a per-wingbeat time scale for isometrically scaled animals. They show that animals may specialize in both maneuverability and stability despite the normal assumption that these two quantities run counter to each other. They also propose that other mechanisms besides yaw could be explained by this phenomenon. The particular turn studied in this paper was a low-speed yaw turn of greater than or equal to 60 degrees. This turn was described as having an angular acceleration phase (with active control) and an angular deceleration phase(with either passive or active control). Traditionally larger animals such as birds are modeled as requiring active deceleration to overcome their larger inertia due to mass while smaller animals such as insects are modeled with significant fluid drag, allowing for passive

deceleration. Considering an animal in hover or low speed flight, damping from wing motion arises from drag created by the flapping motion. When the animal is in full body rotation (yaw), net outside wing velocity is increased on the downstroke and net inside wing velocity increased on the upstroke. This gives rise to a torque that slows the animal's rotation (on both strokes the net torque due to force imbalance acts to slow the rotation). The authors refer to this torque as FCT because it is flapping induced and acts counter to the already present rotation. Hedrick et al. then go on to develop an equation to model FCT and another equation for active deceleration through torque generation. They use the two equations to predict rotational deceleration dynamics and compare these predictions to actual measurements of yaw turning in seven species of flying animals over six orders of magnitude of mass. The FCT model was able to accurately predict yaw deceleration over all seven species (four invertebrate and three vertebrate) while the active model was not able to accurately predict the deceleration rate measured in these species. While active control is possible, the authors contend that the primary mechanism in yaw turn deceleration is passive. Due to these results, maneuverability and stability, often cast in opposition to each other, are more readily optimized together. Essentially, enhancing some factors that enhance maneuverability would also increase FCT, itself an active form of passive stability. One such factor discussed in this paper is wingbeat frequency. Increasing frequency would allow for greater maneuverability and active stabilization as well as increasing FCT through greater force production. This does, however, come with the cost of increases in power requirements to achieve these higher flapping frequencies. The authors also note that while FCT does provide open loop stability, reducing neuromuscular and sensory requirements, it does not eliminate these as FCT results in asymmetric forcing in the wings which suggests neurological input to achieve symmetry of the flapping motion. The authors also discuss the fact that fast forward flight is also likely influenced by FCT but pitching and longitudinal dynamics are known to be inherently unstable in open loop conditions and require active control.

Doman et al. [41] developed a method of controlling a flapping wing micro air vehicle through varying the velocity profiles of each wing. The rotation of the wing is a passive mech-

anism while the stroke motion is actuated using what is termed a Split-Cycle Constant-Period Frequency Modulation. This was accomplished through the use of a split cycle parameter that shifted the peak of the flapping cycle while maintaining the same period. Through theoretical analysis and simulation this method of control is shown the be capable of of control over the vertical and horizontal body forces as well s the rolling and yawing moment when just controlling each wing's flapping frequency and the split cycle parameter. By introducing a bob-weight pitching moment can also be controlled. The controller is implemented using derived sensitivities of cycle-averaged forces and moments (from changes in the wing beat kinematic parameters). These sensitivities are used to formulate a cycle-averaged control law that successfully stabilizes two different models, one using blade-element theory and another based on an empirical unsteady aerodynamic model derived from experiments.

Liu et al. [42] developed a computational framework to provide future guidelines for MAV design. The framework integrated aerodynamics, flight dynamics, structural dynamics, and flight stability and maneuverability applied to hawkmoth and fruit fly models. The aerodynamic model was a fully unsteady Navier-Stokes grid solver coupled to a finite element solver to account for the large deformations of flexible wings (results provided for both rigid and flexible wings). The flight dynamic model is a six-degree-of-freedom set of dynamic equations (Newton-Euler scheme) with translation described in the inertial frame and rotation described in the body frame. In the end, all of these are coupled through a non-linear coupling model and simulated in order to aid in analysis of bio-inspired flight.

Continuing work from [34], Deng et al. [43] present research on flight control algorithms inspired by the top-down architecture of real insects in order to try and preserve high performance aspects despite limited computing power. The hierarchical nature of the model allows for modular construction of the controller, with each module responsible for its own particular task. The independent nature of each module allows for later improvement without redesign of the entire system. The main levels considered are the navigation planner, the flight mode stabilizer and the wing trajectory controller. The navigation planner uses data from sensors and commands to choose the sequence of flight modes necessary to achieve the

mission and navigate the terrain around the vehicle. These flight modes are passed to the flight mode stabilizer which uses inputs from the biomimetic sensors described in Deng [34] to stabilize the various flight modes. It then chooses the necessary forces and torques to achieve this stable configuration and sends them to the wing trajectory controller which chooses the appropriate input voltages for the actuators. The particular advances in this work, at that time, came in the form of the approximation of the time varying aerodynamics as a time invariant system using averaging theory (through assuming the wing-beat frequency is much higher than that of the body motion, meaning that only the mean forces and moments over one aerodynamic period would significantly affect the body dynamics) and in the use of a biomimetic parametrization (such as timing of rotation, stroke angle amplitude, stroke angle offset, etc) of the individual wing paths. These simplifications allow the controller to take take data from on board sensors and voltage inputs to the wing actuators and control the system, without the complication of the controller needing to know the exact aerodynamic model or accurate vehicle morphological parameters.

Oppenheimer et al. [44] use their work from [28] and develop a control strategy to allow the vehicle to hover stably using two wing actuators controlling the angular position of the wing in the stroke plane and a bob weight to move the vehicle center of gravity. The Split-Cycle Constant-Period Frequency Modulation technique is used to generate non zero stroke averaged rolling and yawing moments while the bob weight generates pitching moments and controls translation. The bob weight had to be included as using the Split-Cycle Constant-Period Frequency Modulation technique to generate pitching moments also generated vertical forcing and rolling moments whereas the bob weight could generate the pitching moment independent of other forcing. Expressions for the control derivatives due to variations in the wing beat frequencies, split cycle parameters, and movement of the bob weight are given. Using the stroke-averaged aerodynamic model, a flight control law is generated and then applied to the time varying dynamic model to demonstrate applicability of the stroke averaged model.

Chapter 2

Equations of Motion

In this chapter the equations of motion are derived using quasi coordinate form of the typical Lagrange's equations. The purpose and uses of quasi coordinates are described along with how they are applied to this particular system. The changes to the Lagrange's equation due to the use of quasi coordinates rather than the usual general coordinates are also presented with more detail available in Meirovitch [33]. This is followed by a formulation of the kinetic and potential energy for use in the modified Lagrange's equations (along with the virtual work due to the non-conservative forces). The Lagrange's equations are then fully formulated and transformed into a state space form for ease of use. The wing kinematics used in this system are also described, followed by a check of the linear and angular momentum due to only the inertial loading. The actual physical quantities used to describe this system are provided in Section 5.1.

2.1   Quasi Coordinates

Quasi coordinates are a set of independent coordinates that describe a system uniquely. In the case of a rigid system these coordinates are often those that describe the translation of the body origin and the rotation of the reference axes [33]. In the case of this thesis these
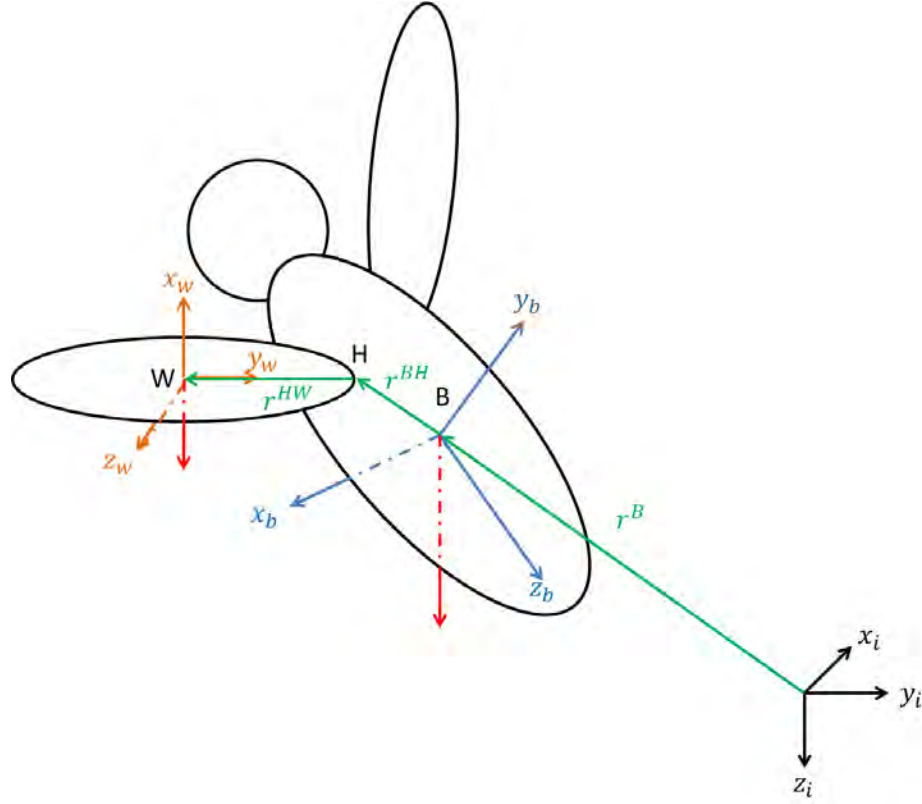
Figure 2.1: Flapping flight system

coordinates are the velocity vector and position vector of the body frame, b, relative to an inertial frame, i, and the angular velocities and angles of the body frame relative to the inertial frame (as described below in Equation 2.1 through Equation 2.4). These coordinates are described as quasi coordinates because the velocities can not be directly integrated to obtain positions/angles.

Figure 2.1 illustrates the system investigated in this thesis. The system is described by several frames including the inertial frame (center at origin, O), i, the body frame (center at body center of mass, B), b, the stroke frame, s, and the wing frame (center at wing center of mass, W), w. Using these frames the quasi coordinates can be described as follows:

$$\{_i\mathbf{r}^B\} = \{_ix^B, _iy^B, _iz^B\}^T \tag{2.1}$$

$$\{\varphi^b\} = \{\Psi^b, \Theta^b, \Phi^b\}^T \tag{2.2}$$

$$\{_b\mathbf{v}^B\} = \{_bu^B,_b v^B,_b w^B\}^T \tag{2.3}$$

$$\{_b\boldsymbol{\omega}^b\} = \{_bp^b,_b q^b,_b r^b\}^T \tag{2.4}$$

Here the left subscript denotes the reference frame the variable is written in while the upper right superscript denotes the point(s) or frame being referenced.

In order to relate the velocities and angular velocities to the position and angles one must first take into account the rotation between the body and inertial frame through the Euler angles described in Equation 2.2. This is a simple 3-2-1 rotation giving rise to the rotation matrix:

$$[\mathbf{T}_{bi}] = \begin{bmatrix} \cos\Psi^b\cos\Theta^b & \sin\Psi^b\cos\Theta^b & -\sin\Theta^b \\ \cos\Psi^b\sin\Theta^b\sin\Phi^b - \sin\Psi\cos\Phi^b & \sin\Psi^b\sin\Theta^b\sin\Phi^b + \cos\Psi^b\cos\Phi^b & \cos\Theta^b\sin\Phi^b \\ \cos\Psi^b\sin\Theta^b\cos\Phi^b + \sin\Psi^b\sin\Phi^b & \sin\Psi^b\sin\Theta^b\cos\Phi^b - \cos\Psi^b\sin\Phi^b & \cos\Theta^b\cos\Phi^b \end{bmatrix} \tag{2.5}$$

and the position and angles are then related to the velocities and angular velocities by:

$$\{_i\dot{\mathbf{r}}^B\} = [\mathbf{T}_{ib}]\{_b\mathbf{v}^B\} \tag{2.6}$$

$$\{_i\dot{\boldsymbol{\varphi}}^b\} = [\mathbf{E}_{bi}]^{-1}\{_b\boldsymbol{\omega}^b\} \tag{2.7}$$

where $\mathbf{E}_{bi}$ is the matrix that relates the body angular rates and the time derivatives of the Euler angles. The derivation of this matrix can be found in the appendix to Bierling [1].

$$[E_{bi}] = \begin{bmatrix} -\sin\Theta & 0 & 1 \\ \sin\Phi\cos\Theta & \cos\Phi & 0 \\ \cos\Phi\cos\Theta & -\sin\Phi & 0 \end{bmatrix} \tag{2.8}$$

For convenience a new plane is defined, the stroke plane, in which the majority of the flapping motion takes place. This plane is explained by Ellington [27] as the plane defined by the wing bases, that is, the root of the wing and the wing tip at its forward and rearmost points. This definition also allows for a differentiation of the stroke plane for each wing which could be necessary for control and maneuvering as shown by Fry [6]. The stroke plane
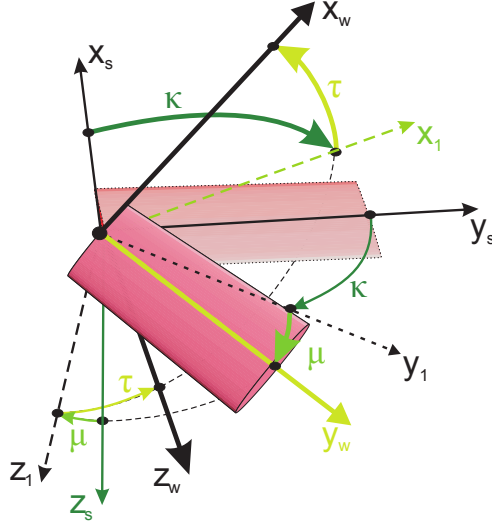
Figure 2.2: Rotation from the stroke frame to the wing frame[1]

is defined by a 2 rotation about the body y axis through the angle δ_r or δ_l (depending on whether it is the right or left wing). Thus the rotation matrix from the body to the stroke frame is:

$$[\mathbf{T}_{sb}] = \begin{bmatrix} \cos\delta & 0 & -\sin\delta \\ 0 & 1 & 0 \\ \sin\delta & 0 & \cos\delta \end{bmatrix} \tag{2.9}$$

The wing frame is then defined relative to the stroke frame by three Euler angles, namely the stroke angle κ, the rotation angle τ, and the deviation angle μ. The rotation itself is a 3-1-2 rotation through κ then μ and finally τ as shown in Figure 2.2. The rotation matrix from the stroke frame to the wing frame is therefore:

$$[\mathbf{T}_{ws}] = \begin{bmatrix} -\sin\kappa\sin\mu\sin\tau + \cos\kappa\cos\tau & \cos\kappa\sin\mu\sin\tau + \sin\kappa\cos\tau & -\cos\mu\sin\tau \\ -\sin\kappa\cos\mu & \cos\kappa\cos\mu & \sin\mu \\ \sin\kappa\sin\mu\cos\tau + \cos\kappa\sin\tau & -\cos\kappa\sin\mu\cos\tau + \sin\kappa\sin\tau & \cos\mu\cos\tau \end{bmatrix} \tag{2.10}$$

The angular velocity of the wing frame and relative to the body frame is given by the sum of the angular velocity of the stroke frame relative to the body frame and the angular velocity of the wing frame relative to the stroke frame (details of this derivation are given by

23

Bierling [1]):

$$\{\boldsymbol{\omega}^{bw}\} = \{\boldsymbol{\omega}^{bs}\} + \{\boldsymbol{\omega}^{sw}\} \tag{2.11}$$

The angular velocity of the stroke frame relative to the body frame is simply:

$$\{_s\boldsymbol{\omega}^{bs}\} = \{0, \dot{\delta}, 0\}^T \tag{2.12}$$

while angular velocity of the wing frame relative to the stroke frame is given in both frames by:

$$\{_s\boldsymbol{\omega}^{sw}\} = \left\{ \begin{array}{c} -\dot{\tau}\sin\kappa\cos\mu + \dot{\mu}\cos\kappa \\ \dot{\tau}\cos\kappa\cos\mu + \dot{\mu}\sin\kappa \\ \dot{\tau}\sin\mu + \dot{\kappa} \end{array} \right\} \qquad \{\boldsymbol{\omega}^{sw}\} = \left\{ \begin{array}{c} -\dot{\kappa}\sin\tau\cos\mu + \dot{\mu}\cos\tau \\ \dot{\kappa}\sin\mu + \dot{\tau} \\ \dot{\kappa}\cos\tau\cos\mu + \dot{\mu}\sin\tau \end{array} \right\} \tag{2.13}$$

Taking the time derivative yields the following vector which will be needed later in the derivation of the equations of motion and the aerodynamic model.

$$\{_w\dot{\omega}^{sw}\} = \left\{ \begin{array}{c} -\ddot{\kappa}\sin\tau\cos\mu - \dot{\kappa}\dot{\tau}\cos\tau\cos\mu + \dot{\kappa}\dot{\mu}\sin\tau\sin\mu + \ddot{\mu}\cos\tau - \dot{\mu}\dot{\tau}\sin\tau \\ \ddot{\kappa}\sin\mu + \dot{\kappa}\dot{\mu}\cos\mu + \ddot{\tau} \\ \ddot{\kappa}\cos\tau\cos\mu - \dot{\kappa}\dot{\tau}\sin\tau\cos\mu - \dot{\kappa}\dot{\mu}\cos\tau\sin\mu + \ddot{\mu}\sin\tau + \dot{\mu}\dot{\tau}\cos\tau \end{array} \right\} \tag{2.14}$$

2.1.1 Quaternions

Quaternions represent an alternative to the traditional Euler angle approach for equations of motion. Utilizing four parameters instead of three, quaternions avoid the gimbal lock problem that Euler angles exhibit as the pitch angle approaches ninety degrees. However, quaternions also exhibit the disadvantage of providing less physical insight due to their abstract nature. In this study quaternions are defined as follows:

$$\bar{\boldsymbol{q}} = q_0 + q_1 i + q_2 j + q_3 k \tag{2.15}$$

The rotation matrix from the body frame to the inertial frame (and visa versa) as well as the kinematic equations can be written in terms of quaternions as described in [45].

$$
T_{bi} = \begin{bmatrix} q_0^2 + q_1^2 - q_2^2 - q_3^2 & 2\left(q_1 q_2 + q_0 q_3\right) & 2\left(q_1 q_3 - q_0 q_2\right) \\ 2\left(q_1 q_2 - q_0 q_3\right) & q_0^2 - q_1^2 + q_2^2 - q_3^2 & 2\left(q_2 q_3 + q_0 q_1\right) \\ 2\left(q_1 q_3 + q_0 q_2\right) & 2\left(q_2 q_3 - q_0 q_1\right) & q_0^2 - q_1^2 - q_2^2 + q_3^2 \end{bmatrix} \tag{2.16}
$$

$$
\dot{\bar{\boldsymbol{q}}} = \begin{bmatrix} -q_1 & -q_2 & -q_3 \\ q_0 & -q_3 & q_2 \\ q_3 & q_0 & -q_1 \\ -q_2 & q_1 & q_0 \end{bmatrix} {}_b\boldsymbol{\omega}^b \tag{2.17}
$$

2.2 Lagrange's Equations for Quasi Coordinates

The derivation of the equations of motion is based on the standard Lagrange's equations. These are usually derived from Hamilton's principle and are valid for a set of generalized coordinates. As this is a well established derivation, it will not be repeated here but more detail is provided in Meirovitch [33]. Typically the standard Lagrange's equations are expressed as:

$$
\frac{d}{dt}\left(\frac{\partial L}{\partial \dot{q}_k}\right) - \frac{\partial L}{\partial q_k} = Q_k \qquad k = 1, 2, ..., n \tag{2.18}
$$

where L is the Lagrangian of the system (difference of the kinetic and potential energy), q_k are the generalized coordinates, and Q_k are the generalized (typically non-conservative) forces.

The system investigated in this thesis is described, however, by a set of quasi coordinates, necessitating that a different form of Lagrange's equations be used. Lagrange's equations as applied to quasi coordinates are derived by Meirovitch [33]. The general form of these equations is as follows:

$$
\frac{d}{dt}\left\{\frac{\partial \bar{L}}{\partial \omega}\right\} + [\beta]^T [\gamma] \left\{\frac{\partial \bar{L}}{\partial \omega}\right\} - [\beta]^T \left\{\frac{\partial \bar{L}}{\partial q}\right\} = \{N\} \tag{2.19}
$$

where q is the generalized coordinate, ω is a quasi coordinate representing of the velocities (cannot be directly integrated to get the positions q), and $\bar{L}$ is the Lagrangian written in a

new form as a function of the coordinates q_k and ω_k. Because the ω's can be written as linear combinations of the $\dot{q}_k$ terms they can be expressed in the form $\omega_s = \alpha_{1s}\dot{q}_1 + \alpha_{2s}\dot{q}_2 + ... + \alpha_{ns}\dot{q}_n$ or:

$$\{\omega\} = [\alpha]^T\{\dot{q}\}, \quad \{\dot{q}\} = [\beta]\{\omega\} \quad (for\ non-singular\ [\alpha]) \tag{2.20}$$

Expressing equation 2.19 in terms of the variables relevant to this system yields:

$$\frac{d}{dt}\left(\frac{\partial L}{\partial\{_b\mathbf{v}^B\}}\right) + \{_b\tilde{\boldsymbol{\omega}}^b\}\frac{\partial L}{\partial\{_b\mathbf{v}^B\}} - [\mathbf{T}_{bi}]\frac{\partial L}{\partial\{_i\mathbf{r}^B\}} = \{_b\mathbf{F}^B\} \tag{2.21}$$

$$\frac{d}{dt}\left(\frac{\partial L}{\partial\{_b\boldsymbol{\omega}^b\}}\right) + \{_b\tilde{\boldsymbol{v}}^b\}\frac{\partial L}{\partial\{_b\mathbf{v}^B\}} + \{_b\tilde{\boldsymbol{\omega}}^b\}\frac{\partial L}{\partial\{_b\boldsymbol{\omega}^b\}} - [\mathbf{E}_{bi}]\frac{\partial L}{\partial\{_i\boldsymbol{\varphi}^B\}} = \{_b\mathbf{M}^B\} \tag{2.22}$$

where L is the Lagrangian of the system and $_b\mathbf{F}^B$ and $_b\mathbf{M}^B$ are the aerodynamic and gravitational forces and moments respectively (expressed in the body frame b). Because all of the bodies in this system are rigid and the gravitational effects are handled as external loads there is no potential energy involved in the Lagrangian calculation. Also, because the kinetic energy is not dependent on the positions $\{_i\mathbf{r}^B\}$ or the angles $\{_i\boldsymbol{\varphi}^B\}$ the corresponding terms in equations 2.21 and 2.22 are both zero. More details on the exact form of the kinetic energy equation follow.

2.2.1   Kinetic Energy Equation

The expression for the kinetic energy is typically given as one half a mass component multiplied by velocity squared. Expanding this into a little more robust form provides the equation:

$$KE = \frac{1}{2}\int \mathbf{V}^T\mathbf{V}dm \tag{2.23}$$

and for this particular system (the equations for the second wing are derived in the same exact manner as for the first):

$$KE = \frac{1}{2}\int \mathbf{V}^{B^T}\mathbf{V}^{B^T}dm_b + \frac{1}{2}\int \mathbf{V}^{W^T}\mathbf{V}^{W^T}dm_w \tag{2.24}$$

After integration this can be condensed to a convenient matrix equation:

$$KE = \frac{1}{2}\{\mathbf{V}^T\}[\mathbf{M}]\{\mathbf{V}\} \tag{2.25}$$

26

In order to preserve this form the vector $\mathbf{V}$ must be enlarged to include the rotational velocity between the body and wing frames. This vector is given by:

$$\{\mathbf{V}\} = \left\{ {}_b\mathbf{v}^{B^T}, {}_b\boldsymbol{\omega}^{b^T}, {}_b\boldsymbol{\omega}^{bw^T} \right\}^T \tag{2.26}$$

This allows us to create a matrix $\mathbf{M}$ as defined below:

$$[\mathbf{M}] = \begin{bmatrix} \mathbf{M}_{11} & \mathbf{M}_{12} & \mathbf{M}_{13} \\ \mathbf{M}_{21} & \mathbf{M}_{22} & \mathbf{M}_{23} \\ \mathbf{M}_{31} & \mathbf{M}_{32} & \mathbf{M}_{33} \end{bmatrix} \tag{2.27}$$

$$[\mathbf{M}_{11}] = m_T[\mathbf{E}] \tag{2.28}$$

where $[\mathbf{E}]$ is the 3x3 identity matrix.

$$[\mathbf{M}_{12}] = m_w \left(-{}_b\tilde{\mathbf{r}}^{BH} - \mathbf{T}_{bw\,w}\tilde{\mathbf{r}}^{HW}\mathbf{T}_{wb} \right) \tag{2.29}$$

$$[\mathbf{M}_{13}] = m_w \left(-\mathbf{T}_{bw\,w}\tilde{\mathbf{r}}^{HW}\mathbf{T}_{wb} \right) \tag{2.30}$$

$$[\mathbf{M}_{21}] = [\mathbf{M}_{12}]^T \tag{2.31}$$

$$[\mathbf{M}_{22}] = {}_b\,\mathbf{I}_B^B + \mathbf{T}_{bw\,w}\mathbf{I}_W^W\mathbf{T}_{wb} + m_w \left(-{}_b\tilde{\mathbf{r}}^{BH} - \mathbf{T}_{bw\,w}\tilde{\mathbf{r}}^{HW}\mathbf{T}_{wb} \right)^T \left(-{}_b\tilde{\mathbf{r}}^{BH} - \mathbf{T}_{bw\,w}\tilde{\mathbf{r}}^{HW}\mathbf{T}_{wb} \right) \tag{2.32}$$

$$[\mathbf{M}_{23}] = \mathbf{T}_{bw\,w}\mathbf{I}_W^W\mathbf{T}_{wb} + m_w \left(-{}_b\tilde{\mathbf{r}}^{BH} - \mathbf{T}_{bw\,w}\tilde{\mathbf{r}}^{HW}\mathbf{T}_{wb} \right)^T \left(-\mathbf{T}_{bw\,w}\tilde{\mathbf{r}}^{HW}\mathbf{T}_{wb} \right) \tag{2.33}$$

$$[\mathbf{M}_{31}] = [\mathbf{M}_{13}]^T \tag{2.34}$$

$$[\mathbf{M}_{32}] = [\mathbf{M}_{23}]^T \tag{2.35}$$

$$[\mathbf{M}_{33}] = \mathbf{T}_{bw\,w}\mathbf{I}_W^W\mathbf{T}_{wb} + m_w \left(-\mathbf{T}_{bw\,w}\tilde{\mathbf{r}}^{HW}\mathbf{T}_{wb} \right)^T \left(-\mathbf{T}_{bw\,w}\tilde{\mathbf{r}}^{HW}\mathbf{T}_{wb} \right) \tag{2.36}$$

The derivatives with respect to the velocities $\mathbf{v}^b$ and $\boldsymbol{\omega}^b$ are as follows:

$$\frac{\partial L}{\partial \mathbf{v}^B} = \frac{1}{2}\left({}_b\mathbf{v}^{B^T}\mathbf{M}_{11} + {}_b\boldsymbol{\omega}^{b^T}\mathbf{M}_{21} + {}_b\boldsymbol{\omega}^{bw^T}\mathbf{M}_{31} \right) + \frac{1}{2}\left(\mathbf{M}_{11b}\mathbf{v}^B + \mathbf{M}_{12b}\boldsymbol{\omega}^b + \mathbf{M}_{13b}\boldsymbol{\omega}^{bw} \right) \tag{2.37}$$

$$\frac{\partial L}{\partial \boldsymbol{\omega}^b} = \frac{1}{2}\left({}_b\mathbf{v}^{B^T}\mathbf{M}_{12} + {}_b\boldsymbol{\omega}^{b^T}\mathbf{M}_{22} + {}_b\boldsymbol{\omega}^{bw^T}\mathbf{M}_{32} \right) + \frac{1}{2}\left(\mathbf{M}_{21b}\mathbf{v}^B + \mathbf{M}_{22b}\boldsymbol{\omega}^b + \mathbf{M}_{23b}\boldsymbol{\omega}^{bw} \right) \tag{2.38}$$

and their time derivatives:

$$
\begin{aligned}
\frac{d}{dt}\left(\frac{\partial L}{\partial \mathbf{v}^B}\right) = \frac{1}{2}&\left({}_b\dot{\mathbf{v}}^{B^T}\mathbf{M}_{11} +{}_b\boldsymbol{\omega}^{b^T}\dot{\mathbf{M}}_{21} +{}_b\dot{\boldsymbol{\omega}}^{b^T}\mathbf{M}_{21} +{}_b\boldsymbol{\omega}^{bw^T}\dot{\mathbf{M}}_{31} +{}_b\dot{\boldsymbol{\omega}}^{bw^T}\mathbf{M}_{31}\right) \\
&+ \frac{1}{2}\left(\mathbf{M}_{11b}\dot{\mathbf{v}}^B + \dot{\mathbf{M}}_{12b}\boldsymbol{\omega}^b + \mathbf{M}_{12b}\dot{\boldsymbol{\omega}}^b + \dot{\mathbf{M}}_{13b}\boldsymbol{\omega}^{bw} + \mathbf{M}_{13b}\dot{\boldsymbol{\omega}}^{bw}\right)
\end{aligned}
\tag{2.39}
$$

$$
\begin{aligned}
\frac{d}{dt}\left(\frac{\partial L}{\partial \boldsymbol{\omega}^B}\right) = \frac{1}{2}&\left({}_b\dot{\mathbf{v}}^{B^T}\mathbf{M}_{12} +{}_b\mathbf{v}^{B^T}\dot{\mathbf{M}}_{12} +{}_b\boldsymbol{\omega}^{b^T}\dot{\mathbf{M}}_{22} +{}_b\dot{\boldsymbol{\omega}}^{b^T}\mathbf{M}_{22} +{}_b\boldsymbol{\omega}^{bw^T}\dot{\mathbf{M}}_{32} +{}_b\dot{\boldsymbol{\omega}}^{bw^T}\mathbf{M}_{32}\right) \\
&+ \frac{1}{2}\left(\mathbf{M}_{21b}\dot{\mathbf{v}}^B + \dot{\mathbf{M}}_{21b}\mathbf{v}^B + \dot{\mathbf{M}}_{22b}\boldsymbol{\omega}^b + \mathbf{M}_{22b}\dot{\boldsymbol{\omega}}^b + \dot{\mathbf{M}}_{23b}\boldsymbol{\omega}^{bw} + \mathbf{M}_{23b}\dot{\boldsymbol{\omega}}^{bw}\right)
\end{aligned}
\tag{2.40}
$$

With these equations it is possible to begin assembling the full form of the Lagrange's equations stated previously in Equations 2.21 and 2.22. It is important to note that the equations of motion also require the external forces and moments. For the purpose of this thesis these would include the gravitational effects and those effects due to the aerodynamics of the wings (the body is not considered to have an aerodynamic affect).

2.2.2   State Space Form

For ease of use the equations of motion are transformed into a state space form in which the body acceleration and body angular acceleration terms are collected on the left hand side of the equation while all others are kept on the right hand side. This yields the following equations:

$$
\mathbf{M}_{11}\dot{\mathbf{v}}^B + \mathbf{M}_{12}\dot{\boldsymbol{\omega}}^b = \mathbf{F}_A + \mathbf{F}_G - \tilde{\boldsymbol{\omega}}^b\frac{\partial L}{\partial \mathbf{v}^B} - \left(\dot{\mathbf{M}}_{12}\boldsymbol{\omega}^b + \dot{\mathbf{M}}_{13}\boldsymbol{\omega}^{bw} + \mathbf{M}_{13}\dot{\boldsymbol{\omega}}^{bw}\right)
\tag{2.41}
$$

$$
\mathbf{M}_{21}\dot{\mathbf{v}}^B + \mathbf{M}_{22}\dot{\boldsymbol{\omega}}^b = \mathbf{M}_A + \mathbf{M}_G - \tilde{\mathbf{v}}^B\frac{\partial L}{\partial \mathbf{v}^B} - \tilde{\boldsymbol{\omega}}^b\frac{\partial L}{\partial \boldsymbol{\omega}^b} - \left(\dot{\mathbf{M}}_{21}\mathbf{v}^B + \dot{\mathbf{M}}_{22}\boldsymbol{\omega}^b + \dot{\mathbf{M}}_{23}\boldsymbol{\omega}^{bw} + \mathbf{M}_{23}\dot{\boldsymbol{\omega}}^{bw}\right)
\tag{2.42}
$$

In simplified terms these equations are of the form of a mass matrix dependent on the kinematic variables (which are periodic with time) multiplied by the state derivatives equal to the forcing function dependent on the states and the kinematic variables:

$$[M(\zeta(t))]\dot{x} = f(x, \zeta(t)) \tag{2.43}$$

Where x are the states and $\zeta(t)$ are the periodic prescribed kinematics.

2.2.3   Center of Gravity Calculation

The center of gravity of the entire system is not centered about the body but rather moves with respect to the body due to the motion of the wing. The position of the center of gravity with respect to the inertial frame is calculated as (following equations only take into account one wing, the second wing is added in the same fashion):

$$_i\boldsymbol{r}^{CG} = \frac{_i\boldsymbol{r}^B m_B +_i \boldsymbol{r}^W m_W}{m_B + m_w} \tag{2.44}$$

Expanding $_i r^W$ into its various components yields:

$$_i\boldsymbol{r}^{CG} = \frac{_i\boldsymbol{r}^B m_B + m_W \left(_i r^B + T_{ib\,b} r^{BH} + T_{ib} T_{bw\,w} r^{HW}\right)}{m_T} \tag{2.45}$$

The kinematic equation for the motion of the center of gravity is simply the derivative of Equation 2.45.

$$_i\dot{\boldsymbol{r}}^{CG} = \frac{T_{ib\,b}\boldsymbol{v}^B m_B + m_W \left(T_{ib\,b}\boldsymbol{v}^B + T_{ib\,b}\boldsymbol{\omega}^b{}_b r^{BH} + T_{ib\,b}\boldsymbol{\omega}^b T_{bw\,w} r^{HW} + T_{ib\,b}\boldsymbol{\omega}^{bw} T_{bw\,w} r^{HW}\right)}{m_T}$$
$$\tag{2.46}$$

2.2.4   Wing Kinematics

The wing kinematics are divided into three main motions, the dominant motion being the stroke (often referred to in terms of the downstroke and upstroke), the rotation of the wing about its axis of rotation (to ensure that the wing is at a positive angle of attack for all or the

majority of the stroke), and the deviation from the stroke plane. As insects do not employ a tail for steering or stabilization, the wing kinematics are of particular importance since they are responsible for the aerodynamic forcing, and passive as well as active stabilization. The focus of this thesis was not to explore the exact kinematics of a particular insect and therefore a more simple approach was used to describe the wing motion and help with physical understanding of the phenomena occurring during flight. In this case a sinusoidal description of the wing motion determined through use of an amplitude, offset, and phase lag captures the necessary motion well enough.

2.2.4.1   Stroke Angle

The stroke angle is the dominant motion of the wing which for many insects is a rowing motion in hover rather than the typical up and downstroke of birds (though some insects such as some butterflies and moths utilize a motion dominated by up and down strokes). In this case the motion is described by the following equation (where ν is the flapping frequency):

$$\kappa = \kappa_0 + \kappa_{max} \cos(2\pi\nu t) \tag{2.47}$$

These variables (κ_0, κ_{max}) are separate for each wing where setting $\kappa_{0,r} = -\kappa_{0,l}$ and $\kappa_{max,r} = -\kappa_{max,l}$ produces a symmetric stroke pattern, an example of which is shown below in Figure 2.3.

2.2.4.2   Deviation Angle

Choosing a frequency twice that of the stroke and rotation provides for the figure eight pattern characteristic of many insect flapping motions. The figure eight pattern is illustrated in Figure 2.4 where it is helpful to note that the stroke plane is the zero line (in z) and all motion above or below this line is due to deviation. In order to produce this motion it is necessary to introduce a phase lag in deviation, ϕ_μ, relative to the stroke angle.
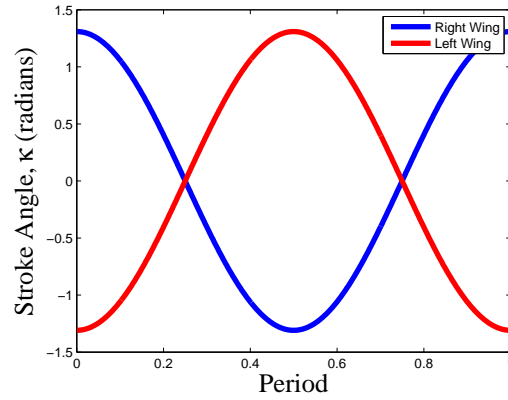
Figure 2.3: Example stroke angle
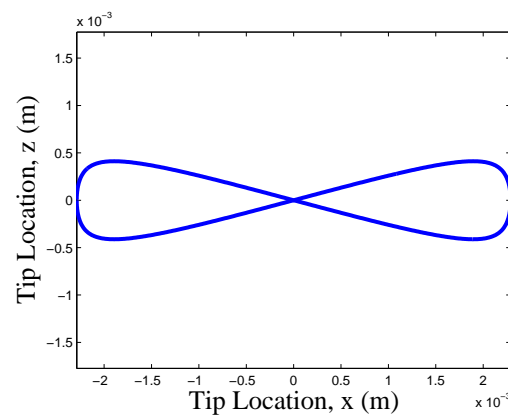
Figure 2.4: Right wing tip location in the x-z plane, showing characteristic figure eight pattern
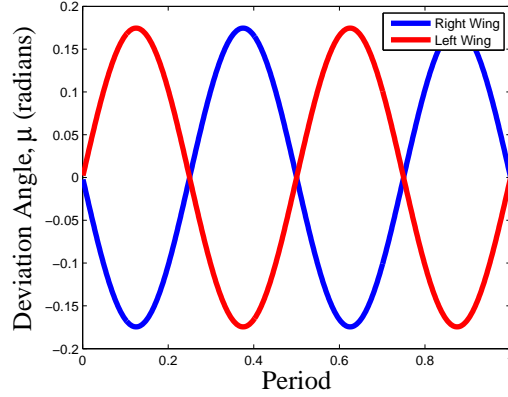
Figure 2.5: Example deviation angle

$$\mu = \mu_0 - \mu_{max}\cos(4\pi\nu t + \phi_\mu) \tag{2.48}$$

Again this motion is separate for each wing and setting $\mu_{0,r} = -\mu_{0,l}$, $\phi_{\mu,r} = \phi_{\mu,l}$ and $\mu_{max,r} = -\mu_{max,l}$ produces a symmetric stroke pattern, an example of which is shown in Figure 2.5.

2.2.4.3   Rotation Angle

The rotation angle produces much of what would typically be considered the geometric angle of attack and is also lagged from the stroke angle, this time by ϕ_τ. This lag allows for advanced or delayed rotation, where a negative phase lag produces an advanced rotation (rotation begins before the stroke reaches the maximum amplitude at the end of each half stroke).

$$\tau = \tau_0 - \tau_{max}\sin(2\pi\nu t + \phi_\tau) \tag{2.49}$$

Separating the motion for each wing involves having different τ_0, τ_{max}, and ϕ_τ where $\tau_{0,r} = \tau_{0,l}$ $\phi_{\tau,r} = \phi_{\tau,l}$ and $\tau_{max,r} = \tau_{max,l}$ produces a symmetric stroke pattern, an example of which is shown in Figure 2.6.
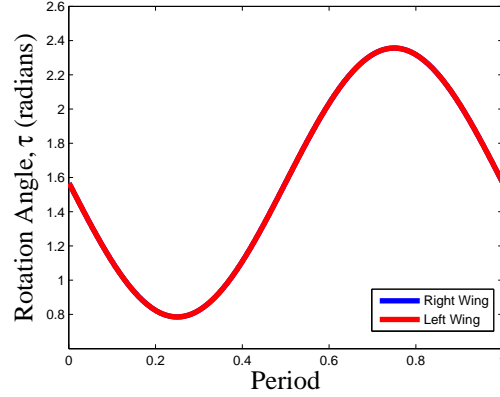
Figure 2.6: Example rotation angle

2.2.5 Conservation of Momentum

Applying the wing kinematics discussed in section 2.2.4 in a vacuum without gravity creates an environment where no external loads are considered. This allows the consideration of the system with only the inertial forcing from the wing motion and can be used for validation the dynamics in vacuum.

The initial condition determines the initial momentum which is conserved because there is no external forcing. Setting the initial state ($\mathbf{v}^B$ and $\boldsymbol{\omega}^b$) equal to zero will give a non-zero initial linear and angular momentum so it is more convenient to first solve for an initial state whereby the linear and angular momentum are equal to zero. The linear and angular momentum equations below are the result of the principles of linear and angular momentum, for more details see Bierling [1].

$$\mathbf{LM} = \mathbf{v}^B \left(m_b + m_w \right) + m_w \left(\boldsymbol{\omega}^b \times \mathbf{r}^{BW} + \boldsymbol{\omega}^{bw} \times \mathbf{r}^{HW} \right) \tag{2.50}$$

$$\mathbf{AM} = \mathbf{I}_B^B \boldsymbol{\omega}^b + \mathbf{I}_W^W \left(\boldsymbol{\omega}^b + \boldsymbol{\omega}^{bw} \right) + \mathbf{r}^{BW} \times \left(\mathbf{v}^B + \boldsymbol{\omega}^b \times \mathbf{r}^{BW} + \boldsymbol{\omega}^{bw} \times \mathbf{r}^{HW} \right) m_w \tag{2.51}$$

Setting these equations equal to zero and solving for the resulting initial state ($\mathbf{v}^B$ and $\boldsymbol{\omega}^b$) gives a point from which time marching can begin. Simulating the system and calculating the resulting linear and angular momentum (in the inertial frame) provides Figures 2.7 and 2.8.
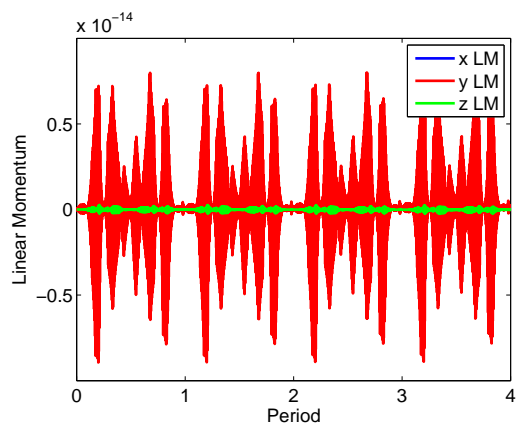
Figure 2.7: Linear momentum in vacuum
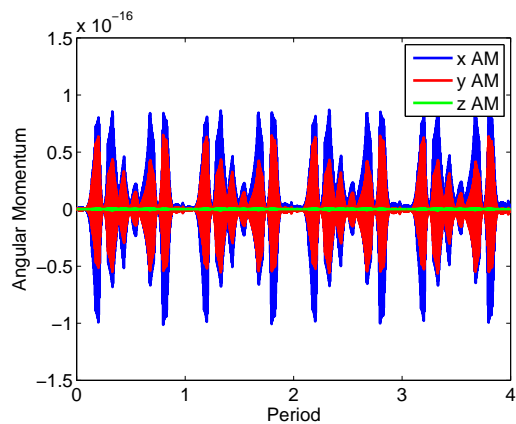
Figure 2.8: Angular momentum in vacuum

This shows that, as expected, the linear and angular momentum are equal to zero withing numerical precision when only inertial forcing is present.

Chapter 3

Aerodynamic Model

As discussed in the literature review, a number of researchers have investigated the aerodynamics of flapping flight. Most have used quasi steady methods [2, 7, 8, 26], computational fluid dynamics (CFD) [38, 10, 46], or a hybrid form of the two. The purpose of this thesis was to create a flight dynamic model for the eventual purpose of controller synthesis and the analysis of flight dynamic metrics such as stability and maneuverability. The aerodynamic models discussed above are inadequate for this application. The quasi steady methods often run efficiently but are not able to fully capture the complicated phenomena surrounding the complex flapping motion. CFD methods are able to capture these phenomena but can take days to run a single period of analysis, much too long for use in a controller. For these reasons it was important to create a reduced order model capable of accurately capturing these phenomena but also one that runs efficiently with run-times more on the order of the quasi steady methods. The airloads model developed by Peters et al. [15] coupled with an assumed inflow model allows for the degree of accuracy necessary while still running in reasonable amounts of time for controller synthesis.

3.1   Airloads Model

Peters' airloads model allows for large frame motion (such as the prescribed motion of the wings) as well as small deformation from this frame. As this thesis deals only with rigid bodies the small deformation component is not used. The airloads model also provides for inclusion of a completely separate inflow model that can be varied independently from the airloads model itself. This allows the quasi steady airloads model to include as detailed a wake (inflow) model as desired, up to and including a fully 3D unsteady wake. Thus by carefully calculating and including all effects it is possible to take what begins as a 2D airloads theory and create a fully encompassing 3D aerodynamic model. The importance here is that this inflow model can be varied to be as accurate and as efficient as desired, all completely separately from the quasi steady airloads model.

The airloads model itself is derived from potential flow and begins with the non-penetration boundary condition due to the velocity from the movement of the airfoil, the freestream flow, and any induced flow (inflow).

$$w = u_0 \frac{\partial h}{\partial x} + \frac{\partial h}{\partial t} + v_0 + v_1 \frac{x}{b} \tag{3.1}$$

where w is the total induced flow, u_0 and v_0 are the velocities of the airfoil in the x and y direction (illustrated in Figure 3.1), v_1 is the velocity gradient, and h terms represent the small deformation from the large frame motion which in the present work are set to zero.

The derivation is presented with more details in Peters et al. [15]. The components of the total induced flow are related to the general airloads.

$$\tau_0 = u_0 \left(w_0 \right) \tag{3.2}$$

$$\tau_1 = b \dot{w}_0 + u_0 w_1 \tag{3.3}$$

$$\tau_2 = \frac{b}{4} \dot{w}_1 \tag{3.4}$$

$$\tau_s = f \tau_0 \tag{3.5}$$
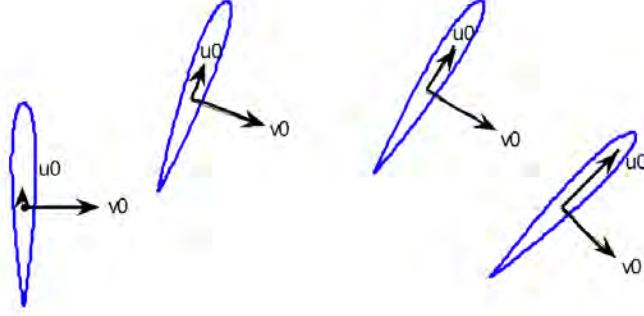
Figure 3.1: Peters' airloads model coordinate system

where f is the reversed flow parameter. These equations are greatly simplified from their original form due to the assumption that all bodies are rigid. This also leads to $w_0 = v_0$ and $w_1 = v_1$ ($w_m = 0$ where $m \geqq 2$). For more detailed equations with deformation terms, see Peters et al. [15]. The velocities of the airfoil with respect to the air, u_0 and v_0 as well as the velocity gradient v_1, are written in the wing frame and are dependent on the fuselage velocity, the prescribed wing velocity with respect to the fuselage, any freestream flow present, and inflow due to shed vorticity.

$$u_0 = -y\dot{\kappa}\cos(\tau) + y\dot{\mu}\sin(\tau) - {}_w\lambda_x + {}_wV_x^B \tag{3.6}$$

$$v_0 = -y\dot{\mu}\cos(\tau) - y\dot{\kappa}\sin(\tau) - {}_w\lambda_y + {}_wV_z^B \tag{3.7}$$

$$v_1 = -b\dot{\tau} - b_w\omega_y^b \tag{3.8}$$

where y is the spanwise location, ${}_w\lambda_x$ is the inflow velocity in the wing x direction, ${}_w\lambda_y$ is the inflow velocity in the wing z direction, ${}_wV_x^B$ is the velocity of the body in the wing x direction, ${}_wV_z^B$ is the velocity of the body in the wing z direction, b is the semi-chord, and

$_w\omega_y^b$ is the angular velocity of the body in the wing y direction. The general airloads can then be resolved into a pressure difference ΔP (again, details in Peters et al. [15]) which is integrated along the chord to get the aerodynamic lift, thrust, and moment in the wing frame (per unit length).

$$L_0 = -2\pi\rho b \left(fu_0v_0 + \frac{1}{2}\left(b\dot{v}_0 + u_0v_1\right)\right) \tag{3.9}$$

$$T = 2\pi\rho b f v_0^2 \tag{3.10}$$

$$L_1 = \pi\rho b \left(u_0v_0 - \frac{1}{2}\frac{b}{4}\dot{v}_1 \right) \tag{3.11}$$

These forces can then be integrated over the span or summed using blade element theory in order to get the total forcing and moment for the entire wing.

3.1.1 Reversed Flow

Reversed flow is the term used to refer to the case when the traditional leading edge is no longer the actual leading edge. In other words, what is usually the trailing edge is leading with respect to the motion of the airfoil. Several studies have been done that illustrate the effectiveness in using reversed flow (through timing of wing rotation with respect to stroke) as a control mechanism [2, 30, 14]. The rotation of the wing can be altered to change the reaction forces caused by the rotational effects. If the wing flips early (before the end of the half stroke) then the resulting total force should be upward. If the flip is late then the resulting force (due to rotational effects) would be a downward force. If the flip spans both half strokes then the resulting downward and upward forces (due to rotational effects) cancel. In Figure 3.2 you can see how the advanced or delayed rotation can add or subtract lift from the case where rotation is symmetric. It is also clear that the trailing edge leads at some points in the stroke. Therefore proper timing of wing rotation on each wing can create a force imbalance that can be used for control [2]. The reversed flow caused by these varying rotations (anytime the trailing edge is leading) is accounted for the the variable f in Equation 3.5. This parameter, f, is called the reversed flow parameter and ensures that the $\Delta P = 0$
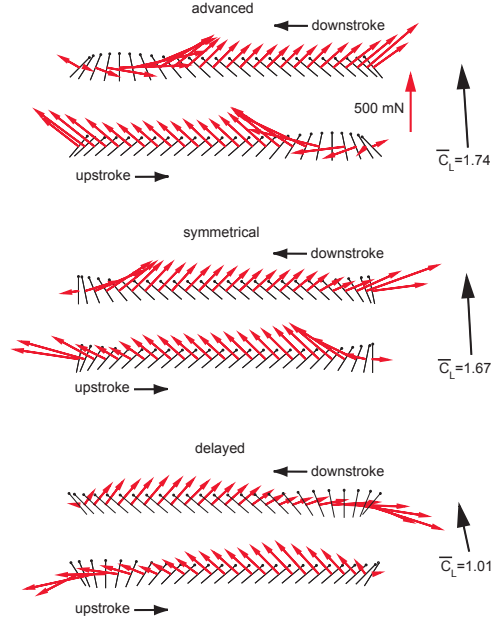
Figure 3.2: Results of alteration to wing flip timing [2]

at the true trailing edge. There are several cases for f:

$$f = 1 \quad \text{(reversed flow neglected)} \tag{3.12}$$

$$f = -1 \quad \text{(trailing edge always at what is normally the leading edge)} \tag{3.13}$$

$$f = \frac{u_0}{|u_0|} \quad \text{(full reversed flow)} \tag{3.14}$$

$$f = \cos(\alpha) \quad \text{(soft reversed flow)} \tag{3.15}$$

where α is the airfoil angle of attack as defined by Peters [15]. In the case of full reversed flow the sign of f changes with the sign of u_0 moving the stagnation point and thus the lift direction. Soft reversed flow makes a smooth transition between these two cases and makes lift proportional to $\frac{\sin(2\alpha)}{2}$ instead of $\sin(\alpha)$.

3.2 Assumed Inflow Models

The quasi-steady airloads model can be coupled with an inflow model to account for the unsteady effects present due to the complicated nature of flapping flight. These inflow mod-

els are completely separate from the airloads model as shown by the separate λ terms in Equations 3.6 and 3.7. Thus different inflow models can be developed and applied to the aerodynamic forcing equations allowing for a wide range of accuracy and efficiency (run time). Theoretically, given a fully 3D inflow that takes into account all the wake effects at all times, one could create a perfect 3D aerodynamic code given the inflow model and the 2D airloads theory. The inflow models discussed below were used in various stages of this thesis work.

3.2.1 Momentum Disk Theory

Helicopter theory often makes use of inflow in calculating aerodynamic loads as well as calculating power and efficiency. A common initial approach to inflow when dealing with helicopters is to assume a constant inflow based on momentum disk theory as detailed by Johnson [47]. Using momentum theory the thrust generated by a helicopter rotor can be related to the induced velocity by the equation:

$$v_h = \sqrt{\frac{T}{2\rho A}} \tag{3.16}$$

where v_h is the inflow, T is the thrust from the rotor, ρ is the density of the air, and A is the area swept by the rotor. The thrust necessary to counteract gravity at trim is just $m_{total}g$. The area swept by the wings is $2\kappa_{max}R_w^2$. This leads to the inflow at hover of:

$$\lambda = \sqrt{\frac{m_{total}g}{4\rho\kappa_{max}R_w^2}} \tag{3.17}$$

Alternatively one can calculate the lift force in the body frame without including inflow and use the average lift over a period as the thrust from the rotor, T.

$$\lambda = \sqrt{\frac{(_bF_A)_z}{4\rho\kappa_{max}R_w^2}} \tag{3.18}$$

Once a new lift force is calculated using this inflow it can be substituted as a new rotor thrust force and the process iterated to a specified convergence condition.

In order to be used in Equations 3.6 and 3.7 this velocity must be rotated into the wing frame and the correct components used.

$$_w \{\lambda_x, \lambda_y, \lambda_z\}^T = [T_{ws}]_s \{0, 0, \lambda\}^T \tag{3.19}$$

3.3 Power Calculations

The power is calculated by using Equations 3.9, 3.10, and 3.11 for each blade element (where η is the blade width) and multiplying them by the wing velocity in the corresponding direction.

$$Power = Tu_0 + L_0 v_0 + L_1 v_1 \tag{3.20}$$

Expanding this equation and simplifying terms yields the equation below:

$$Power = \pi\rho b\eta \left[-b\dot{v}_0 v_0 - \frac{b}{8}\dot{v}_1 v_1 \right] \tag{3.21}$$

Because the velocity functions are periodic they can be expanded using Fourier series (using v_0 without inflow as an example):

$$\dot{v}_0 v_0 = \sum_{n=1}^{\infty} \sum_{m=1}^{\infty} m\omega \left[a_n \cos(n\omega t) + b_n \sin(n\omega t) \right] \left[-a_m \sin(m\omega t) + b_m \cos(m\omega t) \right] \tag{3.22}$$

Integrating these equations over one period to get the average power leads to cancellation of the terms. When n is not equal to m all terms cancel as they are orthogonal. When n is equal to m:

$$\int_{period} \cos(n\omega t) \sin(m\omega t) dt = \int_{period} \cos(n\omega t) \sin(n\omega t) dt = 0 \quad \text{(orthogonal)} \tag{3.23}$$

$$a_n b_m \int_{period} \cos(n\omega t)\cos(m\omega t)dt - a_m b_n \int_{period} \sin(n\omega t)\sin(m\omega t)dt \quad (3.24)$$

$$= a_n b_n \int_{period} \cos^2(n\omega t)dt - a_n b_n \int_{period} \sin^2(n\omega t)dt \quad (3.25)$$

$$= a_n b_n \int_{period} \left[\cos^2(n\omega t) - \sin^2(n\omega t)\right] dt \quad (3.26)$$

$$= a_n b_n \int_{period} \left[\frac{1 + \cos(2n\omega t)}{2} - \frac{1 - \cos(2n\omega t)}{2}\right] dt \quad (3.27)$$

$$= a_n b_n \int_{period} \cos(2n\omega t)dt \quad \text{(which is zero when the period is equal to } \frac{1}{\omega}\text{)} \quad (3.28)$$

The solution for v_1 is of the same form, showing that for periodic velocities without inflow the average power is always zero. This is significant in that if one were to optimize for average power there would not be a solution, emphasizing how important the inflow solution is to this problem. An accurate inflow solution is essential when considering matters of power. If the inflow is included in the power calculations the resulting power is equal to that shown in Equation 3.29.

$$Power = \pi\rho b\eta 2fu_0 v_0 \lambda_y + 2fu_0\lambda_y^2 - 2fv_0^2\lambda_x - 2fv_0\lambda_x\lambda_y + u_0 v_1\lambda_y + \lambda_x\lambda_y v_1 - \frac{b}{8}\dot{v}_1 v_1 \quad (3.29)$$

3.4 Validation

For verifying the aerodynamic model a comparison was made with the quasi steady aerodynamics used in Stanford [3]. Stanford [3] used the 2D quasi-steady model developed by Berman and Wang [26]. The aerodynamics of Berman and Wang [26] are applicable only

to rigid airfoils undergoing large motion. Peters aerodynamics can handle small flexible motions in addition to the large rigid motion but the flexible part is not considered in this work. There are several key differences, however, that must be accounted for before the models can be directly compared. Examining the equations used for the forcing in Berman and Wang [26]:

$$F_{y'_e} = \int_0^L \left[m_{22} \cdot v_{z'_e} \cdot \dot{\psi} + \rho_f \cdot \Gamma \cdot v_{z'_e} - m_{11} \cdot a_{y'_e} - \frac{dF^v_{y'_e}}{dx'_e} \right] \cdot dx'_e \tag{3.30}$$

$$F_{z'_e} = \int_0^L \left[-m_{11} \cdot v_{y'_e} \cdot \dot{\psi} + \rho_f \cdot \Gamma \cdot v_{y'_e} - m_{22} \cdot a_{z'_e} - \frac{dF^v_{z'_e}}{dx'_e} \right] \cdot dx'_e \tag{3.31}$$

$$\Gamma = -0.5 \cdot C_T \cdot c \cdot \sqrt{v_{y'_e}^2 + v_{z'_e}^2} \cdot \sin(2 \cdot \alpha) + 0.5 \cdot C_R \cdot c^2 \cdot \dot{\psi} \tag{3.32}$$

$$\frac{d}{dx'_e} \left\{ \begin{array}{c} F_{y'_e} \\ F_{z'_e} \end{array} \right\} = 0.5 \cdot \rho_f \cdot c \cdot \left(C_D(0) \cdot \cos^2(\alpha) + C_D(\pi/2) \cdot \sin^2(\alpha) \right) \cdot \sqrt{v_{y'_e}^2 + v_{z'_e}^2} \cdot \left\{ \begin{array}{c} v_{y'_e} \\ v_{z'_e} \end{array} \right\} \tag{3.33}$$

Which when converted to the variables used in this work yield:

$$L_0 = -2C_T \rho b \left(u_0 v_0 f + \frac{1}{2} \frac{C_R}{C_T} \left(b\dot{v}_0 + u_0 v_1 \right) \right) \eta - \frac{dF^v_{z'_e}}{dx'_e} \eta \tag{3.34}$$

$$T = 2C_T \rho b f v_0^2 \eta + C_R \rho b v_0 v_1 \eta - \frac{dF^v_{y'_e}}{dx'_e} \eta \tag{3.35}$$

$$and \; f = \frac{u_0}{\sqrt{u_0^2 + v_0^2}} \tag{3.36}$$

Equations 3.34, 3.35, and 3.36 illustrate the key differences in the aerodynamics being used for this work and those presented by Berman [26]. The last terms in Equations 3.34 and
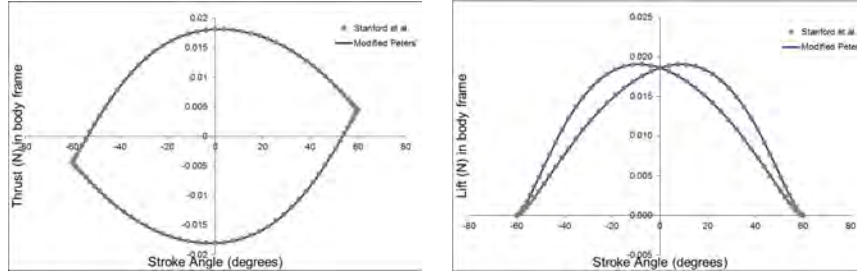
Figure 3.3: Comparison between altered Peters' airloads model and Stanford [3] results

3.35 represent viscous drag terms and for comparison are calculated using the same method presented in Equation 3.33. The C_T and C_R presented in these equations are empirically determined coefficients that can be set to π to agree with Peters theory or the coefficients from Berman [26] for comparison to that work. As seen in Equation 3.36 the reversed flow coefficient must be set to the soft reversed flow condition in order to match the $\frac{\sin(2 \cdot \alpha)}{2}$ trend from Equation 3.32. The study also uses an elliptic wing as defined in Equation 3.37 where c is the chord, $\bar{c}$ is the average chord, y is the span location, and R_w is the overall wing length. The last major difference is the presence of a $v_0 v_1$ term in the thrust where there is not one in Peters theory. This term turns the force due to the $u_0 v_1$ term, usually perpendicular to the wing, and makes it perpendicular to the flow. Also ignored here are the added mass terms in the chord-wise direction. When these terms are set to agree (viscous drag added, coefficients of thrust and rotation equal, added mass ignored, soft reversed flow added, elliptic wing, and $v_0 v_1$ term added) the results are as shown in Figure 3.3 and exhibit exact agreement (the effect of each of the various assumptions is considered further in Section 5.2). The parameters used in this comparison are shown in Table 3.1.

$$c = \frac{4\bar{c}}{\pi \sqrt{1 - \frac{y^2}{R_w^2}}} \tag{3.37}$$

Parameter	Value	Units
ν	26	Hz
R_w	$50 \cdot 10^{-3}$	m
κ_0	0	radians
κ_{max}	$\pi/3$	radians
τ_0	$\pi/2$	radians
τ_{max}	$\pi/4$	radians
ϕ_{tau}	0	radians
μ_0	0	radians
μ_{max}	0	radians
ϕ_μ	0	radians
C_T	1.833	-
C_R	π	-
$C_D(0)$	0.21	-
$C_D(\pi/2)$	3.35	-
$\bar{c}$	$18.2 \cdot 10^{-3}$	m
m_B	$1.648 \cdot 10^{-3}$	kg
m_w	$4.7 \cdot 10^{-5}$	kg

Table 3.1: Parameters used in aerodynamic validation (Figure 3.3)

Chapter 4

Trim and Stability

4.1 Stroke-Averaged System

Since the wing frequencies are much higher than the flight dynamic frequencies, flapping wing aerodynamics on a MAV scale are often approximated on a stroke-averaged basis as these are sufficiently accurate enough on the time scales of the rigid-body dynamics [34, 36]. Here the linearized forcing is determined using perturbations from a reference state to determine Jacobians and initial forcing vectors. In this particular study only symmetric variables are considered.

The system equations are of the form (Subsection 2.2.2):

$$[M(\zeta(t))]\dot{x} = f(x, \zeta(t)) \tag{4.1}$$

One can average the forcing over one flapping cycle for a specified periodic kinematics $\zeta(t)$ and constant prescribed state x_0. This yields an average forcing dependent on kinematic variables, ζ_0, and the state. The kinematic variables, ζ_0 are variables that parametrize the actual kinematics, e.g., κ_0, κ_{max}, τ_{max}, ϕ_τ.

$$f_{avg}(x_0, \zeta_0) = \frac{\int_0^T f(x_0, \zeta(t))dt}{T} \tag{4.2}$$

It is also necessary to average each entry of the mass matrix, $M(\zeta(t))$, for one stroke period. This leads to the stroke averaged system:

$$[M_{avg}]\dot{x} = f_{avg}(x, \zeta_0) \tag{4.3}$$

4.2 Stroke-Averaged Nonlinear Trim

The objective of this section is to determine the trim conditions of the stroke-averaged system by equating the stroke-averaged forces to zero. This leads to no change in the velocity states of the system over a period. Given the stroke-averaged forcing (Equation 4.3) it is possible to solve for a stroke averaged non-linear trim condition. In this case, because the system has been stroke-averaged, the goal of the trim analysis is to get $\dot{x} = 0$ which is equivalent to $f_{avg} = 0$. Since the aerodynamic forces are a nonlinear function of the state variables as well as the control variables, a nonlinear iterative solution technique is required. Here a Newton-Raphson method is used. The Jacobian (derivative of the function with respect to the variables) is calculated using finite difference.

The first set of trim variables, ξ, considered are those of the symmetric states relevant to the aerodynamics and gravity, u, w, q, and Θ (while holding the wing kinematics constant). First it is necessary to calculate the initial stroke-averaged aerodynamic and gravitational forcing vectors, $\boldsymbol{F_{A_0}}$ and $\boldsymbol{F_{G_0}}$ (consisting of the forward forcing X, the vertical forcing Z, and the pitch moment M, as well as a zero in the fourth row from the fourth equation $q = \dot{\theta} = 0$) based on the trim variables. Perturbing each of the entries in the vector ξ and comparing the period averaged forcing to the initial values, $\boldsymbol{F_{A_0}}$ and $\boldsymbol{F_{G_0}}$, provides the the columns of the Jacobians, $\frac{\partial F_A}{\partial \xi}$ and $\frac{\partial F_G}{\partial \xi}$. These Jacobians are in effect the stability derivatives and would correspond, for example, to the slopes of the curves found in Figures 5.6, 5.7, 5.8, and 5.9 if

the initial state were chosen to be the zero state for each of the variables. This provides the average forcing linearized about the trim variables:

$$f_{avg}(x, \zeta_0) = \left[\frac{\partial \boldsymbol{F_A}}{\partial \boldsymbol{x}} \right] \{ \boldsymbol{\Delta \xi} \} + \left[\frac{\partial \boldsymbol{F_G}}{\partial \boldsymbol{x}} \right] \{ \boldsymbol{\Delta \xi} \} + \{ \mathbf{F_{A_0}} \} + \{ \mathbf{F_{G_0}} \} \tag{4.4}$$

It is then possible to solve for a new initial state by iterating the equation:

$$\boldsymbol{\xi_1} = \boldsymbol{\xi_0} - \left[\frac{\partial \boldsymbol{F_A}}{\partial \boldsymbol{\xi}} + \frac{\partial \boldsymbol{F_G}}{\partial \boldsymbol{\xi}} \right]^{-1} (\boldsymbol{F_{A_0}} + \boldsymbol{F_{G_0}}) \tag{4.5}$$

Iteration continues until the error metric (error vector squared) is less than 10^{-10}. In order to prescribe certain motions such as hover, forward flight, and climb, more constraints are needed in the trim analysis. In particular, the derivatives of the vertical and horizontal inertial positions have to be prescribed ($_i\dot{x}_B$ and $_i\dot{z}_B$). This adds two more equations to the system, namely Equations 4.6 and 4.7.

$$_i\dot{x}_B = prescribed \tag{4.6}$$

$$_i\dot{z}_B = prescribed \tag{4.7}$$

This necessitates the use of all four symmetric states and two kinematic variables as trim variables. The kinematic variables chosen for this study as control variables are the stroke offset, κ_0, and the maximum magnitude of rotation, τ_{max}. Otherwise the trim solution is the same as given in Equations 4.4 and 4.5.

4.3 Stroke-Averaged Linearized Stability About Trim

After a trim state has been calculated it is possible to calculate the stability about this trim state by simply taking the eigenvalues of the linearized stability matrix, $\left[\frac{\partial F_A}{\partial x} + \frac{\partial F_G}{\partial x} \right]$, calculated about the trim state. The above matrix is the subset of the matrix computed for the trim solution

4.4 Periodic Trim

Without stroke averaging, the system (Equation 2.43) is a time-varying system. For periodic kinematics, the system becomes a time-varying periodic system. A periodic system can have a periodic trim solution which can calculated using a periodic trim solution technique. The goal of a periodic shooting calculation is to find the initial condition which leads to a periodic solution. The simulation of the system over one period using the initial condition results in a final state equal to the initial one.

$$\mathbf{x}(t_0,\ \mathbf{x}_0) = \mathbf{x}(t_0 + T,\ \mathbf{x}_0) \tag{4.8}$$

As this analysis focuses on the symmetric variables only the longitudinal states are of concern. Because of this only two kinematic variables are needed for control, as stated above. In order to solve for the initial trim state a periodic shooting method is implemented whereby each of the symmetric states is perturbed and time marched through one period of motion and then compared to the unperturbed final state. Stated explicitly, after time marching the initial guess through one period the difference in the final and initial states is the error:

$$x_T^g - x_0^g = error \tag{4.9}$$

$$\text{Where } x_T^g \text{ is } x(T,\ x_0^g) \tag{4.10}$$

The error vector in this case is a non-linear function of the trim variables, ξ. Squaring the error vector gives the error metric by which convergence is determined.

Starting with an initial guess for the trim variables ξ_0, one can iterate using the Newton Raphson scheme to get a trim condition (when the error metric is less than 10^{-18}):

$$x_0 + \frac{\partial x_0}{\partial \xi_0} \Delta \xi = x_T + \frac{\partial x_T}{\partial \xi_0} \Delta \xi \tag{4.11}$$

$$\xi_1 = \xi_0 + \Delta\xi \tag{4.12}$$

It is important to note that, except for the case of completely prescribed kinematics, extra equations (beyond the four state equations) are needed to prescribe the motion of the system as desired. In order to prescribe hover, forward flight, and climb, the averages of the derivatives of the vertical and horizontal inertial positions have to be prescribed $\left(_i\dot{x}_{Bavg}\,and\,_i\dot{z}_{Bavg}\right)$. This adds two more equations to the system, namely Equations 4.13 and 4.14.

$$_i\dot{x}^B_{avg} = \frac{\int_0^T {}_i\dot{x}^B dt}{T} = prescribed \tag{4.13}$$

$$_i\dot{z}^B_{avg} = \frac{\int_0^T {}_i\dot{z}^B dt}{T} = prescribed \tag{4.14}$$

This necessitates the use of all four symmetric states and two kinematic variables as trim variables (same trim variables as the stroke-averaged case).

4.5   Stability of the Periodic System (Floquet Analysis)

To calculate the stability of the system we calculate the state transition matrix. The state transition matrix gives the effect of perturbation (about the trim) in the initial state on the state at the end of one period. If the perturbation grow then we have instability otherwise we have a stable system. In order to do this we perturb each of the states in the initial condition, x_0, and use the perturbation in the resulting solutions at the end of one period to form the columns of the state transition matrix ϕ. Note that this matrix is a subset of the matrix calculated for trim calculations based on periodic shooting. For stability we have $\phi = e^{AT}$ where the eigenvalues of A determine the stability of the system.

Chapter 5

Results

5.1   System Parameters

The system parameters used in this study are altered Manduca sexta parameters derived from [48, 49, 50] and are listed below in Table 5.1. The vehicle itself is not meant to be an exact representation of the Manduca sexta but only based on one, and so the values may be slightly different than those found in literature. There are also crucial differences in that the body is modeled as an ellipsoid and the wings are rectangular. These parameters may also be varied in specific portions of this work as described throughout.

Symbol	Parameter	Value	Units
m_B	Body mass	$1.780 \cdot 10^{-3}$	kg
m_w	Wing mass	$2.133 \cdot 10^{-5}$	kg
I_B^B	Body inertia tensor	Equation 5.1	$kg \cdot m^2$
I_W^W	Wing inertia tensor	Equations 5.2, 5.3	$kg \cdot m^2$
r^{BH}	Vector from the body CG to the hinge point	Equations 5.4, 5.5	m
r^{HW}	Vector from the hinge point to the wing CG	Equations 5.6, 5.7	m
$\bar{c}$	Average chord	0.019427	m
R_w	Wing length	0.05055	m
S_w	Wing area	$0.98203 \cdot 10^{-3}$	m^2
ν	Flapping frequency	25	Hz

Table 5.1: Morphologic parameters

Assuming an ellipsoid body with body length (46.377 mm) and radius (5.93 mm) from [48, 49] provides a body inertia tensor as shown in Equation 5.1.

$$_b I_B^B = \begin{bmatrix} 77.821 & 0 & 0 \\ 0 & 77.821 & 0 \\ 0 & 0 & 2.5307 \end{bmatrix} \cdot 10^{-8} \; kg \cdot m^2 \tag{5.1}$$

Assuming rectangular wings using the parameters shown in Table 5.1 provides the right and left wing inertia tensors.

$$_{w_r} I_{W_r}^{W_r} = \begin{bmatrix} 4.5421 & 0 & 0 \\ 0 & 0.67084 & 0 \\ 0 & 0 & 5.2129 \end{bmatrix} \cdot 10^{-9} \; kg \cdot m^2 \tag{5.2}$$

$$_{w_l} I_{W_l}^{W_l} = \begin{bmatrix} 4.5421 & 0 & 0 \\ 0 & 0.67084 & 0 \\ 0 & 0 & 5.2129 \end{bmatrix} \cdot 10^{-9} \; kg \cdot m^2 \tag{5.3}$$

No data was found for the vectors from the body CG to the hinge so the values in Equations 5.4 and 5.5 were assumed where appropriate.

$$_br^{BH_r} = [0,\ 5.58,\ -10]^T \cdot 10^{-3}m \tag{5.4}$$

$$_br^{BH_l} = [0,\ -5.58,\ -10]^T \cdot 10^{-3}m \tag{5.5}$$

Assuming rotation about the midchord and the rectangular wing profile provides the following hinge to wing CG vectors for the right and left wings.

$$_wr^{HW_r} = [0,\ 0.025275,\ 0]^T m \tag{5.6}$$

$$_wr^{HW_r} = [0,\ -0.025275,\ 0]^T \cdot 10^{-3}m \tag{5.7}$$

5.2 Effects of Model Assumptions on Aerodynamic Forcing

As mentioned in Sections 3.2 and 3.4 there are many different modeling considerations when trying to accurately model the complex flapping wing system of a flapping wing MAV. In this section the effect of some of these models on the aerodynamic forcing will be examined. The parameters used were the system parameters described above with kinematics as shown in Table 5.2.

Parameter	Value (degrees)
κ_0	0
κ_{max}	0.9594
τ_0	$\pi/2$
τ_{max}	1.4667
ϕ_τ	0
μ_0	0
μ_{max}	0
μ_ϕ	0

Table 5.2: Kinematic Parameters

5.2.1 Effect of Reversed Flow
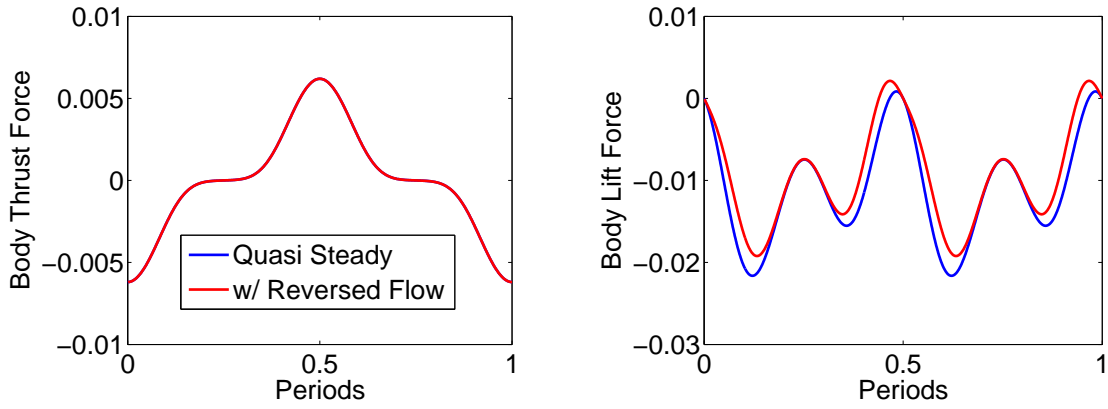
Figure 5.1: Comparison of aerodynamic forcing curves showing the effect of adding reversed flow

Figure 5.1 shows the effect of adding soft reversed flow (defined in Section 3.1.1) to the quasi-steady aerodynamic model. Examining the body frame forcing curves in Figure 5.1 shows that adding reversed flow does not affect the body frame thrust force in an average or an instantaneous sense but it does reduce the magnitude of the body lift force at all times during the period. This is to be expected given that the inclusion of soft reversed flow

switches the trend of lift from $\sin(\alpha)$ to $\frac{\sin(2\alpha)}{2}$. The soft reversed flow also explains the double peaks per half stroke in the body lift curves. As the wing rotates down from ninety degrees the lift increases up until the point it reaches forty-five degrees at which point it begins to reduce again. at the middle of the half stroke it reaches a minima before increasing its as it increases in angle of attack again. Towards the end of the half stroke the lift magnitude again reduces as the angle of attack moves from forty-five degrees back to ninety. This same pattern repeats on the other half stroke.

5.2.2 Effect of Empirical Coefficients
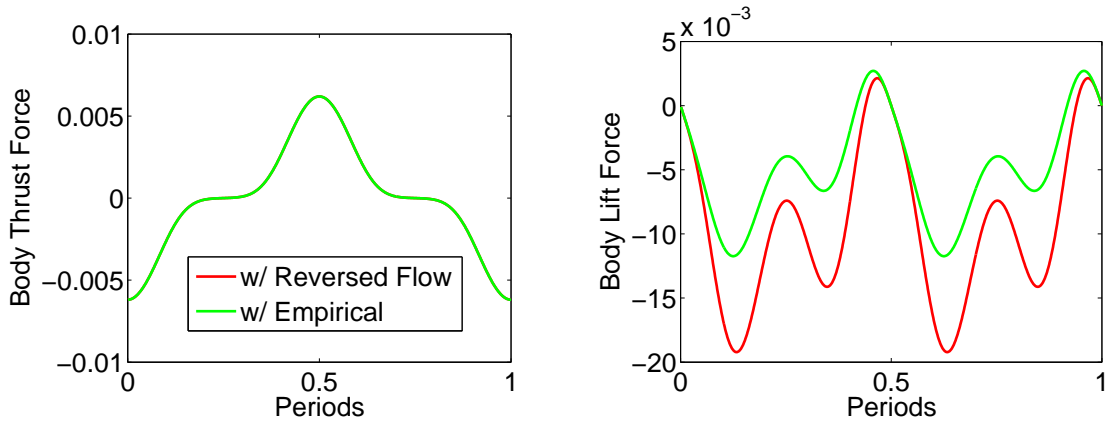
Figure 5.2: Comparison of aerodynamic forcing with the addition of empirical constants

Figure 5.2 shows the results of adding the empirical coefficients $C_T = 1.678$ shown in Equations 3.34 and 3.35 to the results obtained in Section 5.2.1. Adding the empirical coefficient into the forcing model again does not have an effect on the body frame thrust force but does have a significant affect on the body lift force. Decreasing the coefficient of thrust relative to the coefficient of rotation puts more emphasis on the rotational portions of the wing frame lift and thrust equations and decreases the overall magnitude of the forcing.

5.2.3 Effect of Viscosity
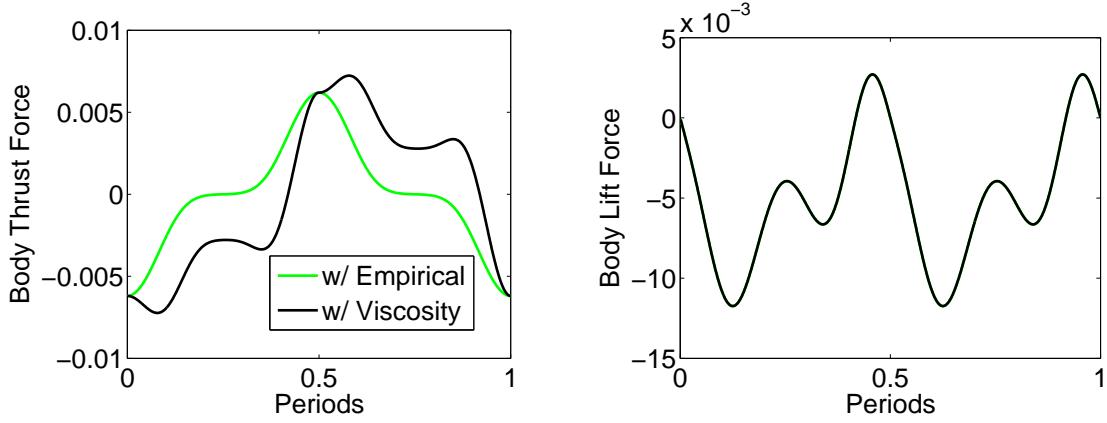
Figure 5.3: Comparison of aerodynamic forcing with the addition of viscosity

Figure 5.3 shows that effect of adding the viscous forcing shown in Equations 3.34 and 3.35 to the results obtained in Section 5.2.2. The addition of viscosity changes only the instantaneous body thrust. It increases drag for both the forward and backward stroke increasing the power required. It does not affect the stroke-averaged thrust as its effects in the body frame due to the forward stroke are canceled by those on the back stroke.

5.2.4 Effect of $v_0 v_1$ Term
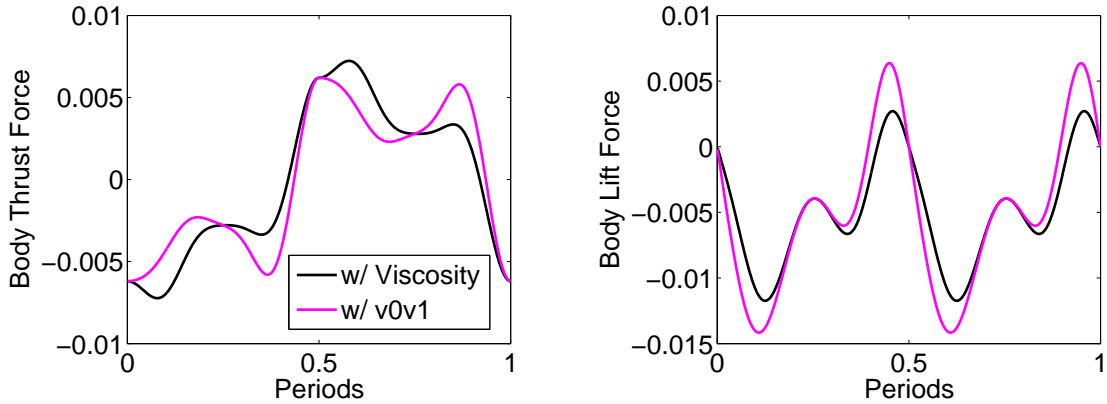
Figure 5.4: Comparison of aerodynamic forcing curves with the addition of the $v_0 v_1$ term

Figure 5.4 shows the effect of adding the $v_0 v_1$ term shown in Equation 3.35 to the results obtained in Section 5.2.3. It shows that while adding the $v_0 v_1$ term to Equation 3.35 does affect instantaneous forcing values in the body frame it does not affect the overall averages over the period.

5.2.5 Inflow
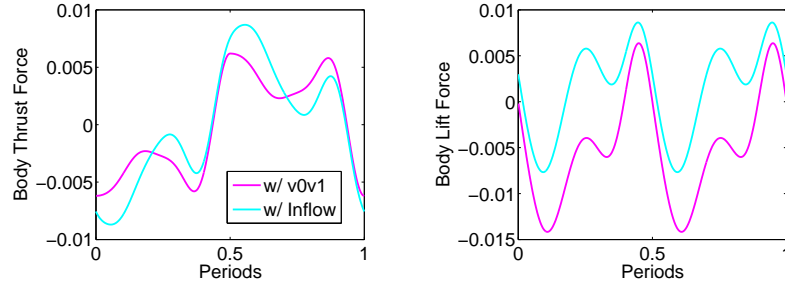
Figure 5.5: Comparison of aerodynamic forcing curves with the addition of inflow

Figure 5.5 shows the effect of adding the prescribed inflow as discussed in Section 3.2 to the results obtained in Section 5.2.4. It can be seen that adding a constant inflow model does not affect the overall average of the body thrust but does affect both body thrust and lift instantaneously and reduces the stroke average of the body lift force due to the energy lost in the wake.

5.3 Nominal System Dynamics

The nominal case consists of a system utilizing the system parameters discussed in Section 5.1. The aerodynamics utilize soft reversed flow but do not include viscous drag or inflow. All time marching was accomplished using the MATLAB program ode45 using a relative tolerance of 10^{-10} and an absolute tolerance of 10^{-15}.

5.3.1 Influence of State Variables on Forcing

The effect of state and potential kinematic control variables (particularly κ_0, κ_{max}, τ_0, and τ_{max}) is examined over the course of a stroke cycle (stroke-averaged forcing). The slopes of the resulting data can be interpreted as aerodynamic (stability and control) derivatives. Both symmetric and antisymmetric variations are considered though it is important to note that the kinematics and geometry are symmetric so changes in the symmetric state variables can only lead to symmetric load variations (though not necessarily vice versa). Using the nominal case (reversed flow, no empirical coefficients, no inflow, no viscous drag, no deviation, AC above the body CG), and a hover trim condition, the results are as shown below in Figures 5.6, 5.7, 5.8, and 5.9. For display purposes the velocities, forces, and moments are normalized by the characteristic velocity, force, and moment as described in Equations 5.8, 5.9, and 5.10.

$$\bar{V} = 2R_w\nu\sin(\kappa_{max}) \tag{5.8}$$

$$\bar{F} = \rho\bar{V}^2 S_w \tag{5.9}$$

$$\bar{M} = \rho\bar{V}^2 S_w\bar{c} \tag{5.10}$$
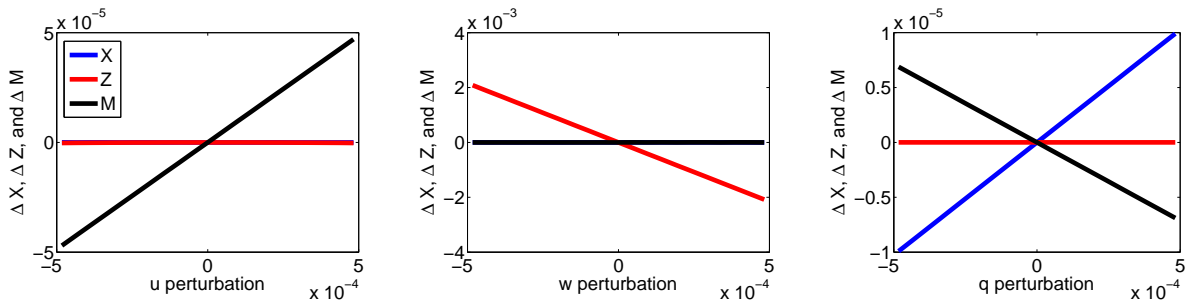
Figure 5.6: Influence of longitudinal variables on longitudinal forcing

Figure 5.6 shows the variation in the symmetric aerodynamic loads (x direction force X^B, z direction force Z^B, and pitching moment M^B) due to perturbation in the symmetric

velocities. The velocity perturbation in the x direction, u^B, leads to little change in loads other than the pitching moment, M^B. Due to the lack of any viscous drag forces there is no change in x direction force (as seen later), force in the z direction experiences a similar lack of change because increase in the force from increased velocity in one direction are offset by decrease in forcing while flapping in the opposite direction. The significant moment effect is due to the fashion in which 2-D pitching moment, L_1, is calculated in Equation 3.11. The u_0v_0 term leads to an additive effect on the forward and backward stroke, for example, if the perturbation is positive then the increase in these two quantities on the forward stroke leads to an increased pitching moment. On the reverse stroke a decrease in both of these terms means that the L_1 quantity does not cancel and a net pitch up results (after rotation into the body frame).

When perturbing velocity in the z direction the only significant affect is a change in the vertical force Z^B. An increase in upward velocity lowers the effective angle of attack and thereby decreases the vertical force, effectively acting as a damper for the motion.

Perturbing the pitch rate produces a significant pitch damping as well as a change in the x direction forcing. Perturbing pitch in a positive direction increases the angle of attack when the wings are rear of the CG and decreases it when forward of the CG. This effectively produces a pitch down moment, damping out the pitch perturbation (the opposite of this effect is present with a negative pitch perturbation, again damping out the motion). The x direction forcing perturbation arises from the u_0v_1 term found in Equation 3.3. Without an equivalent v_0v_1 term as found in Berman and Wang [26] the forcing vector that results from this u_0v_1 term is perpendicular to the wing rather than to the flow. Therefore effective angle of attack changes result in forward forcing when pitch is perturbed.
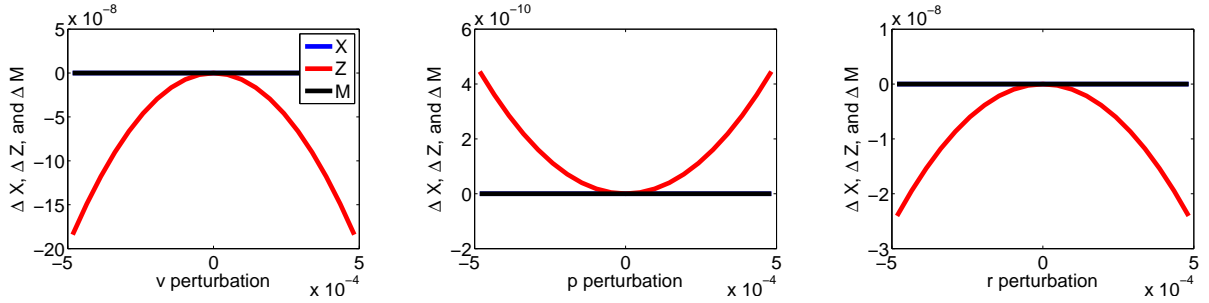
Figure 5.7: Influence of lateral variables on longitudinal forcing

Figure 5.7 shows the effect of lateral motion on longitudinal forces (y direction force Y, roll moment L, and yaw moment N), especially the z direction force. These effects, however, appear to be small when compared with those shown in Figures 5.6 and 5.8. Particularly the changes in forces and moments due to roll are very small and could be neglected.
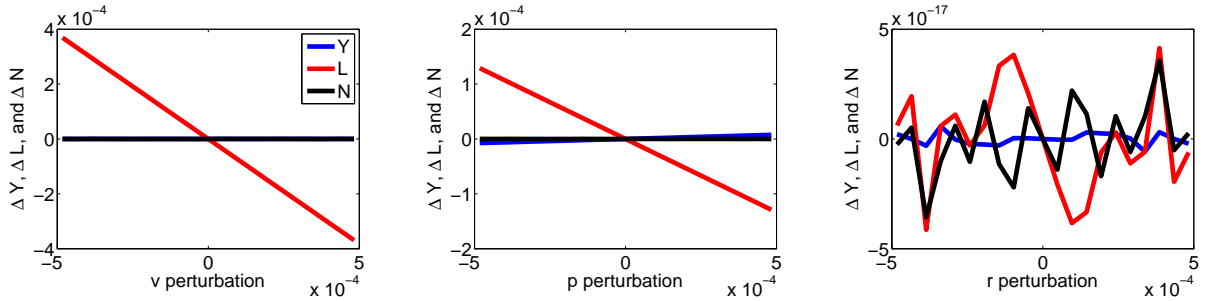
Figure 5.8: Influence of lateral variables on lateral forcing

Figure 5.8 shows the effect of lateral velocity perturbations on the lateral aerodynamic loads. A positive perturbation in the y velocity leads to a significant negative rolling moment. This moment is due to the increase in effective angle of attack on the right wing (the wing toward which the body is moving) and the corresponding decrease in angle of attack of the left wing. This leads to a net negative rolling moment. The lack of a yaw as well as side force damping is due to the absence of viscous drag force in this model.

A significant roll damping is present while all side force and yaw damping is negligible.
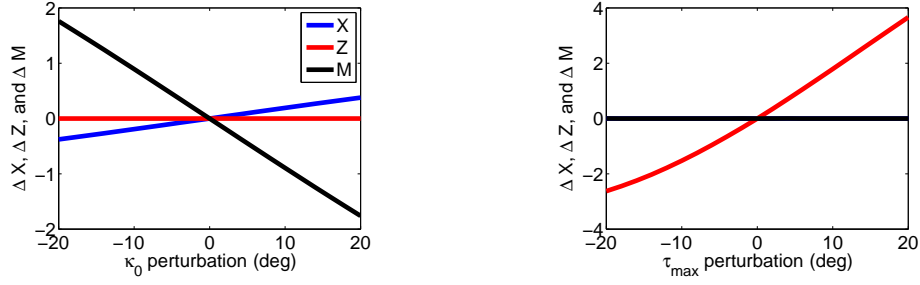
Figure 5.9: Influence of control variables on longitudinal forcing

In Figure 5.9 the effect of the two control variables demonstrates how the vehicle can be controlled for symmetric motion. κ_0 perturbations yield pitching moments because the mean location of forcing is shifted forward or back from the CG (positive κ_0 shifts the wings center of motion further back). This allows for pitch control, which also yields inertial x direction control as the vehicle can be tipped forward or backward and then z body direction forces increased or decreased to achieve inertial x direction movement. The change in z direction forcing is achieved by altering the τ_{max} kinematic variable. This changes the effective angle of attack of the wing.

5.3.2 Stroke-Averaged Nonlinear Trim

The trim condition resulting from using prescribed kinematics ($\kappa_0 = 0$, $\kappa_{max} = 0.95944$, $\tau_0 = \pi/2$, $\tau_{max} = \pi/4$, and no deviation) are shown in Table 5.3. As seen in the table, there are at least four possible trim conditions which where found by starting the iterative nonlinear solution at different initial guesses.

State	Trim Value	State	Trim Value	State	Trim Value	State	Trim Value
u	-1.7759e-15	u	-2.4840e-16	u	2.4680e-15	u	5.9715e-17
w	-3.6136	w	1.7177	w	4.7524	w	-7.2844
q	0	q	0	q	0	q	0
Θ	1.4234e-15	Θ	-1.2207e-16	Θ	3.1416	Θ	3.1416
(a)		(b)		(c)		(d)	

Table 5.3: Multiple sets of trim variables for prescribed kinematics

In Table 5.3 it is clear from the first set of data that in order to maintain a constant state with the given kinematics, the vehicle enters a constant climb in order to counteract the extra lift generated by the wings. The other states remain at basically zero with no forward motion or pitching. In the third set of data the vehicle is flipped over as seen from the Θ value. This state corresponds to a flipped over constant descent which, while not that interesting physically, illustrates a second trim condition for the same kinematic variables. Two more possible trim states are shown in set (b) and (d). The multiple trim conditions are a result of nonlinear lift curve slope, specifically the fact that the lift initially increases with effective angle of attack, reaches a peak at 45° and then decreases. The vehicle z velocity leads to change in effective angle of attack and thus one may find multiple solutions to the trim problem.

Instead of prescribing the control variables, one can prescribe the trim state and calculate the control variables. The trim variables for hover, climb (1 m/s), and forward flight (1 m/s) are shown in Table 5.4. κ_0 tilts the mean position of the wings (majority of the stroke motion) forward or backward of the center of gravity of the system providing pitch control (effectively the elevator when compared to traditional control surfaces). τ_{max} alters the magnitude of the vertical force produced by the wings as shown in Figure 5.9 and effectively acts as the engine, controlling forward or upward velocity depending on pitch.

Variable	Trim Value
u	0
w	0
q	0
Θ	2.7121e-15
κ_0	6.9195e-15
τ_{max}	1.4784

(a)

Variable	Trim Value
u	-1.7576e-16
w	-1
q	0
Θ	-1.7576e-16
κ_0	-1.2832e-16
τ_{max}	1.2522

(b)

Variable	Trim Value
u	1.0000
w	0.001200
q	0
Θ	0.001200
κ_0	0.003644
τ_{max}	1.5015

(c)

Table 5.4: Trim variables for prescribed states: (a) Hover (b) Climb (c) Forward Flight

In order to maintain a hover state it is necessary for the vehicle to alter the lift magnitude from the conditions seen in Table 5.3 so that it just counteracts the force of gravity acting on the body and wings. As the hinge point is directly at the center of gravity no κ_0 change is necessary to balance the pitching moment and only τ_{max} is changed, being increased to reduce the effective angle of attack and thereby the lift force as seen in Table 5.4 (a).

In Table 5.4 (b) the climb condition shows similar trim variables to those of the hover condition but with a reduced τ_{max} in order to increase the upward force as shown in Figure 5.9.

The forward flight case in (c) shows a u not quite equal to one and a w not quite equal to zero as those are the body velocities and the inertial velocities were the ones prescribed as described above. The body is also tipped so that the forcing vector can be realigned. In this particular solution the body is tipped back and the forward and downward velocity combine to create an inertial forward only velocity. In order to allow the body to move in this manner κ_0 is used as a pitch control to pitch the body and τ_{max} is increased slightly, reducing the forcing magnitude to the needed levels. While physically it seems odd to tip backward to move forward, the inertial forward velocity changes the angle of attack of the wing such that the aerodynamic forcing still cancels the gravitational force appropriately.

The addition of the forward velocity also creates a pitch up moment (Figure 5.6) which can only be counteracted by the vehicle pitching back and using gravity to counteract the moment. The tip back would not be possible with viscous effects which would force the vehicle to tip forward to counteract the viscous drag (as discussed later).

5.3.3 Stroke-Averaged Linearized Stability About Trim

Eigenvalues
-0.009238 + 0.005345i
-0.009238 - 0.005345i
-0.009118
0.006210

(a)

Eigenvalues
-0.009901
0.006250 + 0.009158i
0.006250 - 0.009158i
0.01126

(b)

Eigenvalues
-0.003819 + 0.008713i
-0.003819 - 0.008713i
0.01159
0.01174

(c)

Eigenvalues
-0.02662
-0.009801
0.001548 + 0.008993i
0.001548 - 0.008993i

(d)

Table 5.5: Multiple sets of eigenvalues for prescribed kinematics

Table 5.5 shows the eigenvalues of the system at the four trim conditions presented in Table 5.3. All cases show instability about the trim condition as indicated by the positive eigenvalues.

Eigenvalues
-0.01056
-0.004422
0.002210 + 0.003718i
0.002210 - 0.003718i

(a)

Eigenvalues
-0.01190
-0.004867
0.001388 + 0.003279i
0.001388 - 0.003279i

(b)

Eigenvalues
-0.01117
-0.001363 + 0.003563i
-0.001363 - 0.003563i
0.003129

(c)

Table 5.6: Eigenvalues for prescribed states: (a) Hover (b) Climb (c) Forward Flight

Table 5.6 show the eigenvalues for the hover, climb and forward flight trim cases presented in Table 5.4. Again all of these states show instability about trim which is supported by the previous work of Bierling [1] and Richter [51]. The transition between hover and climb can be examined through the root locus plot shown in Figure 5.10 and the transition between hover and forward flight similarly in Figure 5.11.
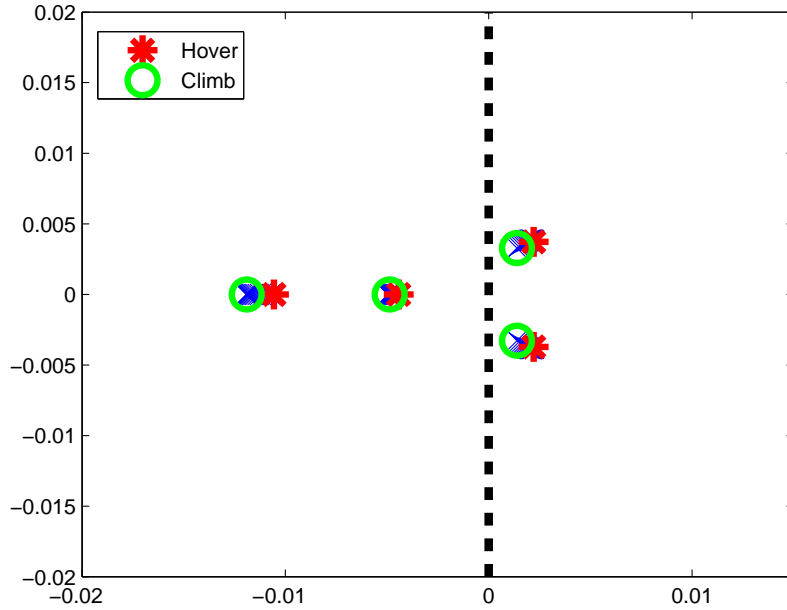
Figure 5.10: Root locus plot showing the transition from hover to climb

65
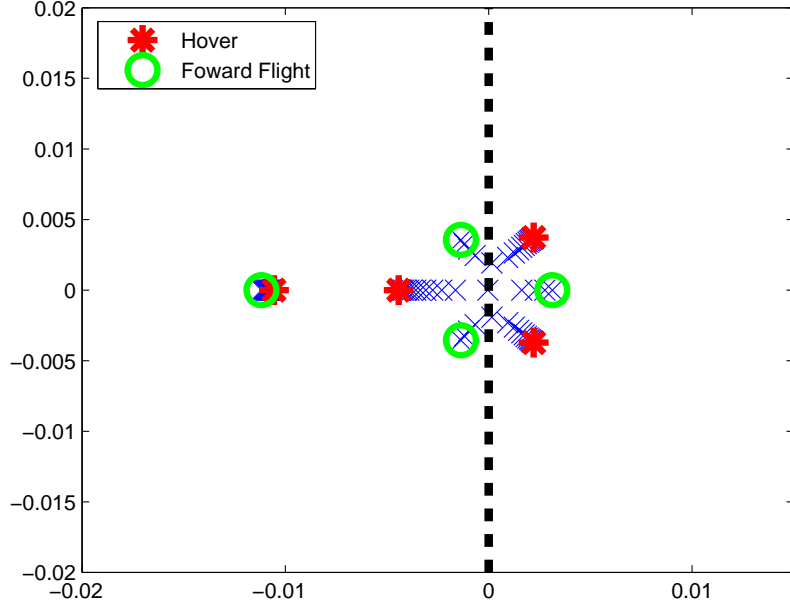
Figure 5.11: Root locus plot showing the transition from hover to forward flight

When looking at the transition from hover to climb all eigenvalues maintain their sign meaning that those that are stable remain stable and those that are unstable remain unstable. In the case of hover transitioning to forward flight, the two oscillatory eigenvalues that are unstable in hover move to stable values for forward flight while one of the stable real eigenvalues becomes unstable.

5.3.4 Periodic Trim

The actual periodic time-varying system has a periodic trim. This trim is calculated by periodic shooting as described in Section 4.4. In the case of prescribed kinematics ($\kappa_0 = 0$, $\kappa_{max} = 0.95944$, $\tau_0 = \pi/2$, $\tau_{max} = \pi/4$, and no deviation) the trim variables consist only of the four symmetric states and the resulting trim conditions are shown below in Figure 5.7. The tables show the trim variables which are the initial values for the states. The tables also show the stroke-averaged values at trim.

State	Trim Value	Average
u	0.1037	2.0063e-08
w	-3.4746	-3.4976
q	1.7521	1.2979e-06
Θ	0.01998	3.2286e-09

(a)

State	Trim Value	Average
u	-0.01347	3.3569e-10
w	1.6621	1.6553
q	-0.6694	-1.7268e-08
Θ	-0.002547	-1.3051e-10

(b)

State	Trim Value	Average
u	0.3757	4.8539e-09
w	4.5879	4.5965
q	7.2558	2.8861e-06
Θ	3.1057	3.1416

(c)

State	Trim Value	Average
u	-0.3542	6.6106e-09
w	-7.09407	-7.1227
q	-1.9779	1.3349e-07
Θ	3.1394	3.1416

(d)

Table 5.7: Multiple sets of trim variables for prescribed kinematics

Providing the initial conditions in Table 5.7 results in a periodic response with average values as shown. When considering that the maximum states are on the order of 10^0 these average trim states compare favorably to those found for the stroke-averaged system shown in Table 5.3.

Prescribing states and allowing two of the kinematic variables to vary in order to achieve hover, climb, and forward flight provide the results shown in Table 5.8. Averaging the states over one period when providing these trim variables provides a better comparison to the stroke-averaged system and results are shown beside their initial value. As in the prescribed kinematic case the averaged values (and the corresponding trim kinematic variables) compare favorably with those of the stroke averaged system shown in Table 5.4.

Variable	Trim Value	Average
u	0.0004158	-1.2196e-12
w	0.01501	-6.8662e-06
q	0.4592	3.0978e-09
Θ	0.01387	2.6342e-12
κ_0	2.5644e-13	
τ_{max}	1.4667	

(a)

Variable	Trim Value	Average
u	0.03585	7.6309e-10
w	-0.9795	-1.0000
q	1.2189	4.0828e-07
Θ	0.01687	9.0399e-10
κ_0	-1.4761e-12	
τ_{max}	1.2382	

(b)

Variable	Trim Value	Average
u	1.002468	0.9996
w	0.07567	0.0056
q	1.3743	5.7435e-007
Θ	0.02025	0.0057
κ_0	0.01006	
τ_{max}	1.4914	

(c)

Table 5.8: Trim variables for prescribed states: (a) Hover (b) Climb (c) Forward Flight

While the forward and vertical velocities listed in Table 5.8 (c) are not one and zero respectively this is because they are body direction velocities. When they are rotated to the inertial directions the horizontal velocity and vertical velocity are $_i\dot{x}_B = 1.0000$ and $_i\dot{z}_B = -4.0172 \cdot 10^{-4}$ respectively.

5.3.5 Stability of the Time-Varying System

Eigenvalues
-0.008955
-0.007726
0.003259 + 0.006159i
0.003259 - 0.006159i

(a)

Eigenvalues
-0.007239
0.008161 + 0.02242i
0.008161 - 0.02242i
0.009764

(b)

Eigenvalues
0.001406 + 0.02622i
0.001406 - 0.02622i
0.003368
0.01096

(c)

Eigenvalues
-0.009036
-0.0081775 + 0.04753i
-0.0081775 - 0.04753i
-0.002184

(d)

Table 5.9: Multiple sets of eigenvalues for prescribed kinematics

All of the trim states in Table 5.7 are unstable as demonstrated by their positive eigenvalues shown in Table 5.9 except for the final trim state which has only negative eigenvalues. Comparing these eigenvalues to the analogous cases found for the stroke-averaged system (shown in Table 5.5) it is clear that the stroke-averaged and time-varying (periodic) systems are not completely interchangeable. While they do have some similarities (such as trim conditions and averaged response) their stabilities are not necessarily the same. In both cases they show the majority of trim conditions to be unstable, the only difference being that the periodic system shows one trim condition to be stable.

Eigenvalues
-0.008955
-0.007726
0.003259 + 0.006156i
0.003259 - 0.006156i

(a)

Eigenvalues
-0.01008
-0.004870
0.0001577 + 0.002010i
0.0001577 - 0.002010i

(b)

Eigenvalues
-0.01541
-0.001014
0.002956 + 0.003488i
0.002956 - 0.003488i

(c)

Table 5.10: Eigenvalues for prescribed states: (a) Hover (b) Climb (c) Forward Flight

As in the prescribed kinematic case the eigenvalues of the time-varying system are on the same order as those of the stroke-averaged system but are not similar otherwise. This points to the fact that the stroke-averaged system is not a direct replacement for the time-varying system despite the fact that the flapping frequency is much higher than the frequency of the body dynamics.
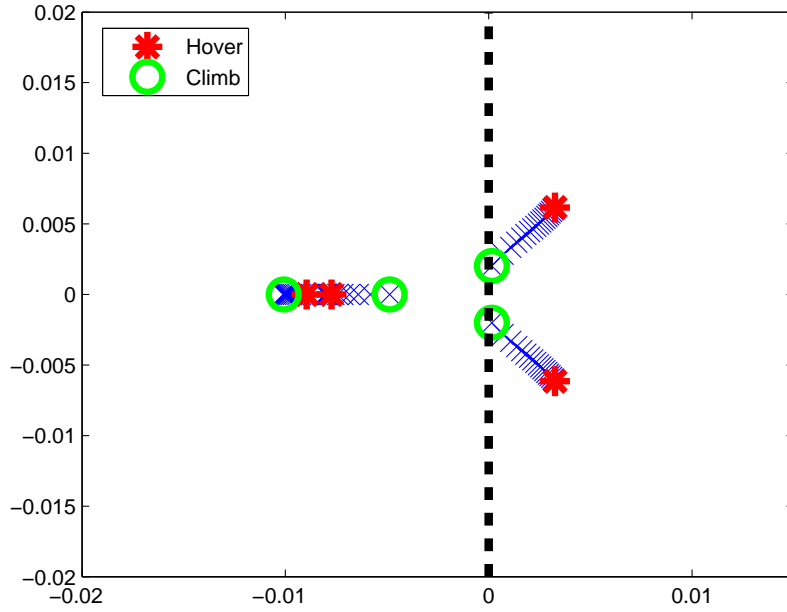
Figure 5.12: Root locus plot showing the transition from hover to climb
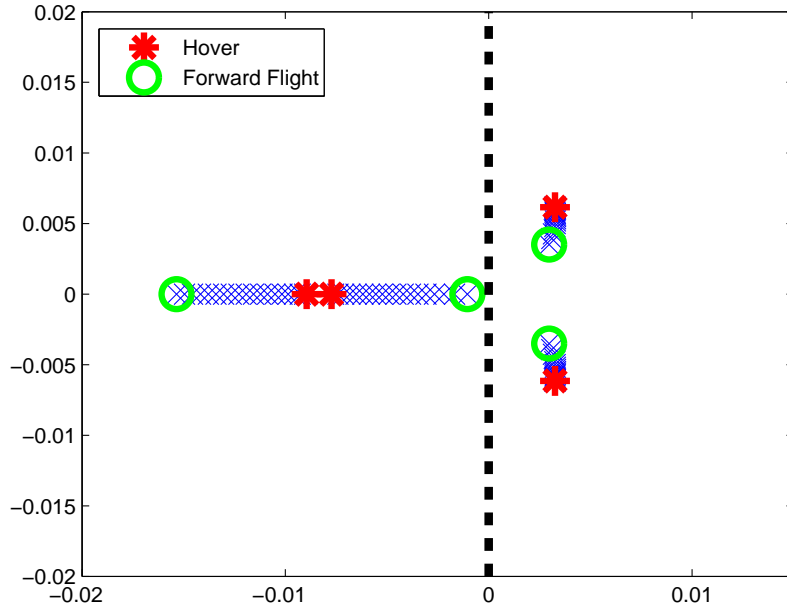
Figure 5.13: Root locus plot showing the transition from hover to forward flight

The transition from hover to climb and hover to forward flight in Figures 5.12 and 5.13 both show that the system remains unstable through the entirety of both transitions. Also those eigenvalues that are stable remain stable and those that are unstable remain unstable. While the exact paths and values are not replicated in the stroke averaged case some of the general trends do appear in both cases. For instance, in the case of the transition between hover and climb, the eigenvalues with real and imaginary components decrease their magnitude (for both the real and imaginary parts) in both the stroke-averaged and time-varying cases.

Because these trim conditions are unstable perturbation from these conditions will cause the system to move away from the periodic trim.

As an example Figure 5.14 shows the hover trim for the nominal periodic system perturbed by one percent of each value shown in Table 5.8 (a). The body velocities at first stay near the trim condition but as the instability due to the perturbation grows they quickly move

away from the trim condition.

Figure 5.14: Perturbed Nominal Hover Trim

5.4 Inflow

The first model added for comparison is a prescribed inflow model as described in Subsection 3.2.1. This constant inflow is based on momentum disk theory and provides a const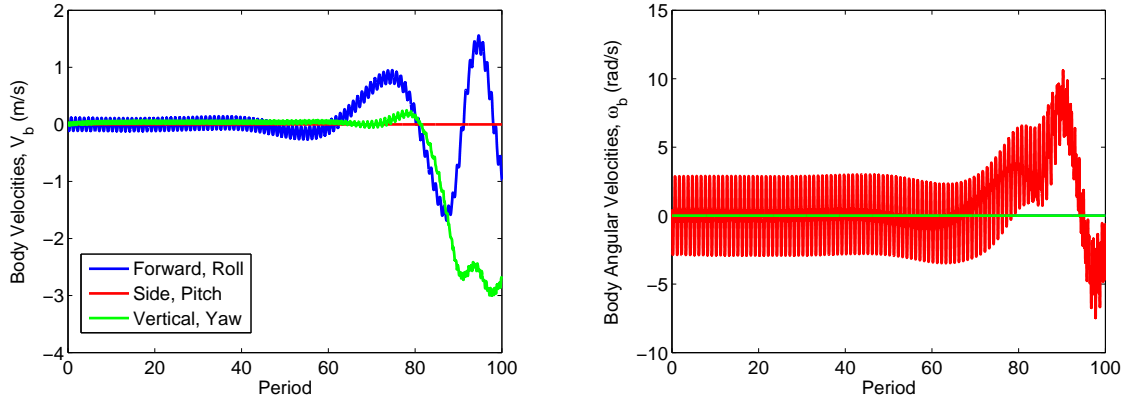ant downwash velocity (in the body frame). This provides a first level approximation of the unsteady portions of the flow that would contribute to the aerodynamics.

5.4.1   Periodic Trim

Variable	Trim Value	Average
u	0.02154	-4.5330e-11
w	0.01509	-2.8670e-05
q	0.9363	1.0289e-07
Θ	0.01520	3.4166e-10
κ_0	7.1690e-13	
τ_{max}	1.1881	

(a)

Variable	Trim Value	Average
u	0.04655	1.9149e-09
w	-0.9818	-1.0000
q	1.3176	5.7236e-07
Θ	0.01674	2.1190e-09
κ_0	6.4085e-11	
τ_{max}	0.9849	

(b)

Variable	Trim Value	Average
u	1.01260	0.9862
w	-0.07876	-0.1627
q	2.1133	1.6284e-06
Θ	-0.1470	-0.1634
κ_0	-0.01033	
τ_{max}	1.1966	

(c)

Table 5.11: Trim variables for prescribed states: (a) Hover (b) Climb (c) Forward Flight

In comparing the trim values for the nominal case with a constant inflow model to those of the nominal case, some interesting similarities arise. The trends for all three states are similar in that forward flight had the highest rotation magnitude in both cases while climb had the lowest (other states remained similar as well) which makes sense given that the same states were prescribed for the both cases. It is also interesting to note that all of the prescribed states showed lower values of max rotation indicating that a geometric angle of attack was needed, given the same states, to counteract the decrease in angle of attack due to prescribed inflow. The forward flight case here shows a stroke-averaged tip forward rather than the tip

backward of the nominal case which is easier to grasp conceptually.

5.4.2   Stability of the Time-Varying System

Eigenvalues
-0.01009
-0.003805 + 0.003115i
-0.003805 - 0.003115i
0.002389

(a)

Eigenvalues
-0.009184
-0.006871 + 0.01053i
-0.006871 - 0.01053i
0.005937

(b)

Eigenvalues
-0.01767
-0.003195 + 0.006549i
-0.003195 - 0.006549i
0.008247

(c)

Table 5.12: Eigenvalues for prescribed states: (a) Hover (b) Climb (c) Forward Flight

Table 5.12 presents the eigenvalues of the system with prescribed inflow. In both Figures 5.15 and 5.16 those eigenvalues that are stable remain stable and those that are unstable remain unstable.
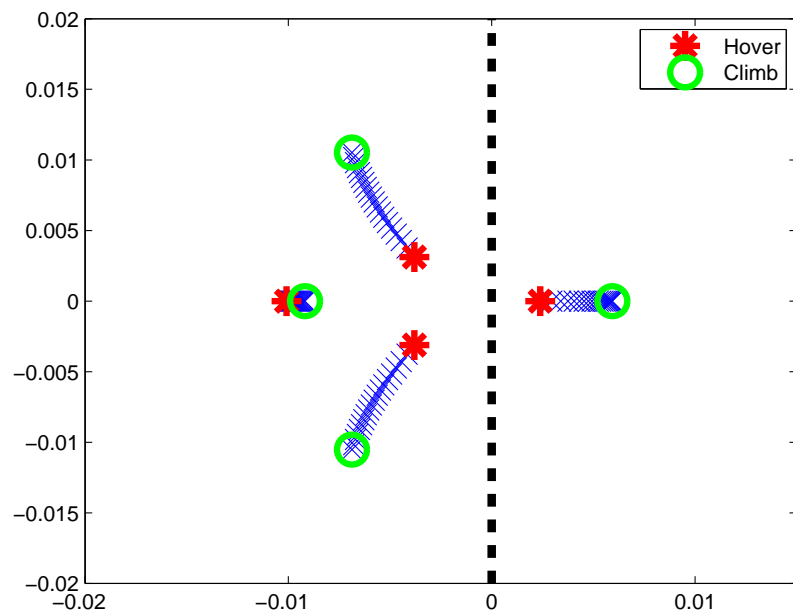
Figure 5.15: Root locus plot showing the transition from hover to climb
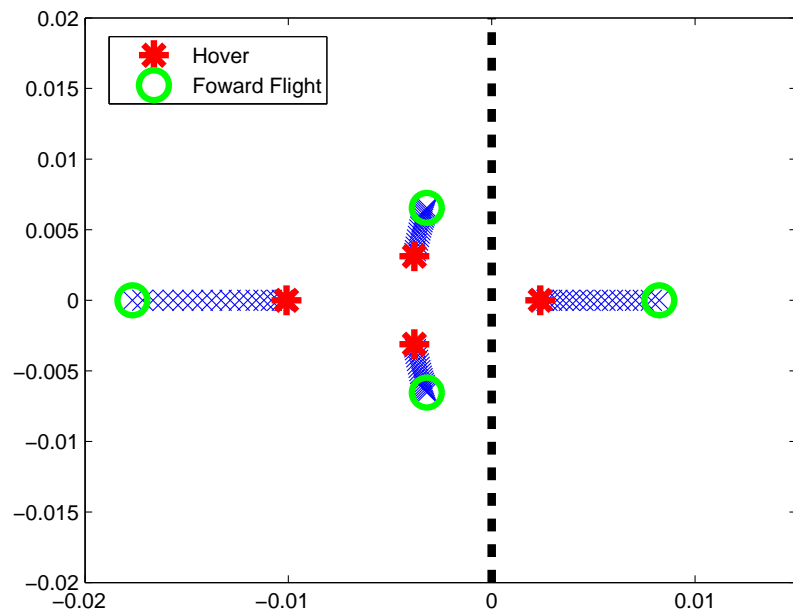
Figure 5.16: Root locus plot showing the transition from hover to forward flight

Examining Figure 5.17 shows that the values for the eigenvalues of the various climbs with inflow are near those of climb without inflow at the inflow speed (-1.23022591896135 m/s). This makes sense as inflow is analogous to climb in many ways. The values are not going to be exact, however, as the inflow is modeled to be in the body z direction at all times where as climb is in the inertial z direction.
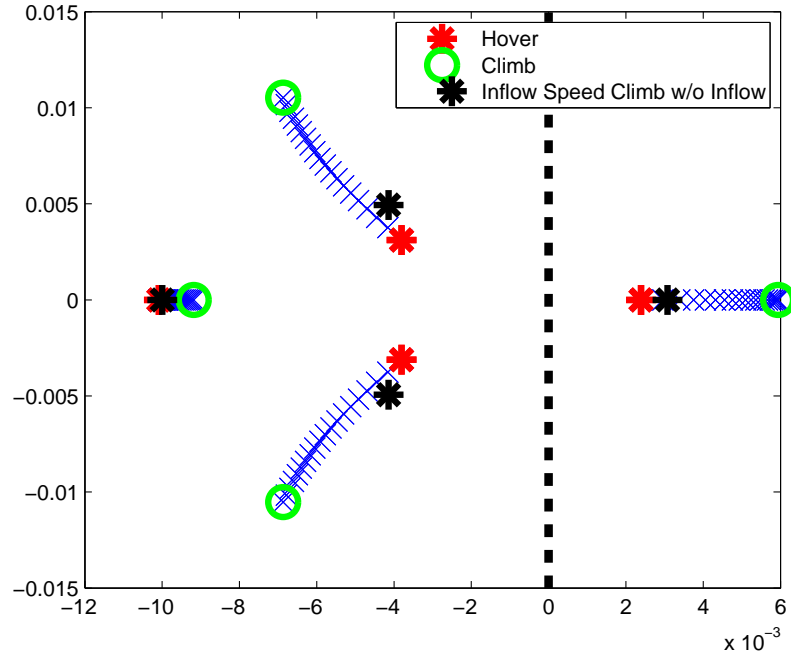
Figure 5.17: Root locus plot showing the transition from hover to climb with a 2 m/s climb (w/o inflow)

5.5 Viscous Drag Effects

This section adds a viscous drag model to the nominal case as described in Equations 3.33, 3.34, and 3.35. The assumed drag constants are $C_D(0) = 0.07$ and $C_D(\pi/2) = 3.06$ which match the hawkmoth empirical parameters provided by Berman [26].

5.5.1 Periodic Trim

Variable	Trim Value	Average
u	0.02353	-6.3107e-11
w	0.01507	-1.5980e-05
q	0.9983	1.8235e-07
Θ	0.01390	4.1235e-10
κ_0	2.8213e-11	
τ_{max}	1.4673	

(a)

| Variable	Trim Value	Average
u	0.09253	-1.2566e-08
w	-0.9794	-1.0000
q	2.3854	-5.7279e-07
Θ	0.01340	2.1154e-09
κ_0	-8.1659e-10	
τ_{max}	1.1523	

(b)

Variable	Trim Value	Average
u	1.02438	0.9893
w	-0.06986	-0.1431
q	2.03599	3.6671e-07
Θ	-0.1286	-0.1436
κ_0	-0.04407	
τ_{max}	1.4592	

(c)

Table 5.13: Trim variables for prescribed states: (a) Hover (b) Climb (c) Forward Flight

The only significant change shown between the nominal case trim variables and those of the nominal case with viscous drag are the initial pitch velocity values which are significantly higher for the nominal case with viscous drag. It is interesting to note that even with viscous drag the maximum rotation angles do not change a great deal in magnitude (only a few percent of their nominal case values) to overcome the viscous effects. This indicates that using the current models assumed in this study, inflow (unsteady effects) seem to have a much larger effect on the overall motion of the body for these three prescribed states. The forward flight case exhibits a similar tip forward to the inflow case, which in the case of

viscous effects is necessary. The forward flight of the vehicle causes extra drag on the forward stroke as compared to back stroke and therefore the lift vector must be tipped forward to counteract this force.

5.5.2   Stability of the Time-Varying System

Eigenvalues
-0.01069
-0.006397 + 0.008184i
-0.006397 - 0.008184i
0.007932

(a)

Eigenvalues
-0.01357
-0.009158 + 0.01531i
-0.009158 - 0.01531i
0.007203

(b)

Eigenvalues
-0.01918
-0.004635 + 0.007753i
-0.004635 - 0.007753i
0.01132

(c)

Table 5.14: Eigenvalues for prescribed states: (a) Hover (b) Climb (c) Forward Flight

Unlike in the case of trim, viscosity changes the stability of the nominal model significantly. The eigenvalues for the nominal case with viscous drag show more similarity with those of the nominal case with inflow (Table 5.12) than those of just the nominal case (Table 5.10). If the root locus plots (Figures 5.18 and 5.19) are examined however, neither case shows the same trends as the nominal case with viscous drag. Also similar to the nominal case with inflow (Figures 5.15 and 5.16), the nominal case with viscous drag shows a larger imaginary magnitude (on those eigenvalues with imaginary parts) than the nominal case (Figures 5.12 and 5.13) alone. In the case of moving from hover to climb this magnitude grows while moving from hover to forward flight sees a slight reduction. In both transitions from hover those eigenvalues that are stable remain stable and those that are unstable remain unstable.
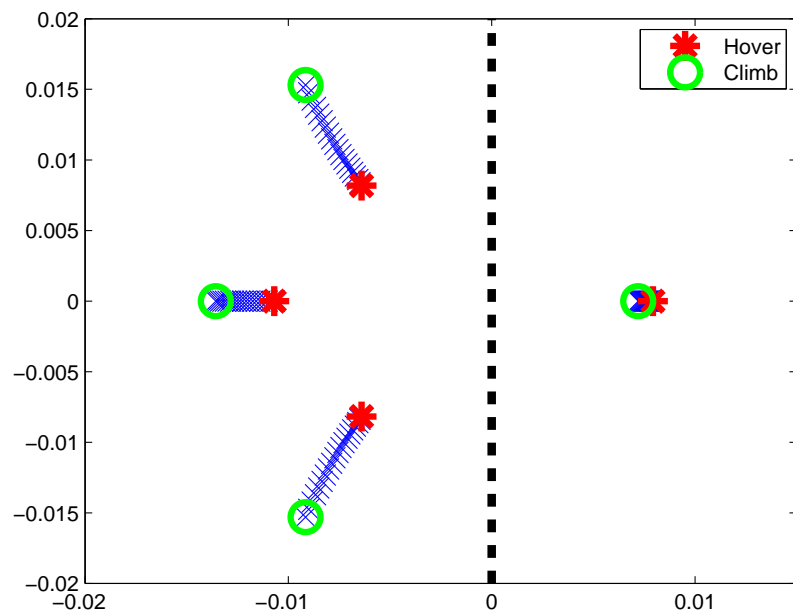
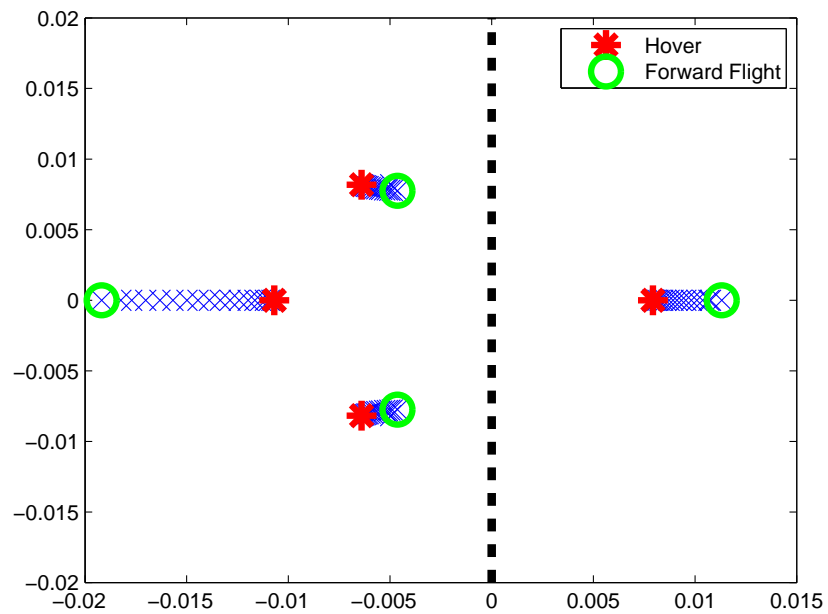Figure 5.18: Root locus plot showing the transition from hover to climb

Figure 5.19: Root locus plot showing the transition from hover to forward flight

5.6 Deviation

This section adds deviation from the stroke plane to the kinematic motion. The added kinematic values are $\mu_0 = 0$, $\mu_{max} = -0.1744$, and $\phi_\mu = \pi/2$.

5.6.1 Periodic Trim

Variable	Trim Value	Average
u	0.01635	-8.8938e-11
w	0.03643	-2.2226e-04
q	1.7920	3.2974e-07
Θ	0.005028	1.8819e-10
κ_0	1.7747e-10	
τ_{max}	1.08971	

(a)

Variable	Trim Value	Average
u	0.03606	4.9307e-10
w	-0.9586	-1.0000
q	2.2421	5.3350e-07
Θ	0.01036	7.1291e-10
κ_0	4.2675e-11	
τ_{max}	0.9557	

(b)

Variable	Trim Value	Average
u	1.01450	0.9988
w	0.05214	-0.0427
q	2.5756	2.0669e-06
Θ	-0.03650	-0.0425
κ_0	0.04563	
τ_{max}	1.1253	

(c)

Table 5.15: Trim variables for prescribed states: (a) Hover (b) Climb (c) Forward Flight

The addition of deviation does make a few changes to the trim conditions produced for hover, climb, and forward flight. As seen in Table 5.15 the forward flight case shows a tip forward similar to that seen in the cases with inflow and viscous effects added. Also the

max rotation angle is decreased (increasing the geometric angle of attack). The addition of deviation removes body lift over the majority of the stroke as seen in Figure 5.20.
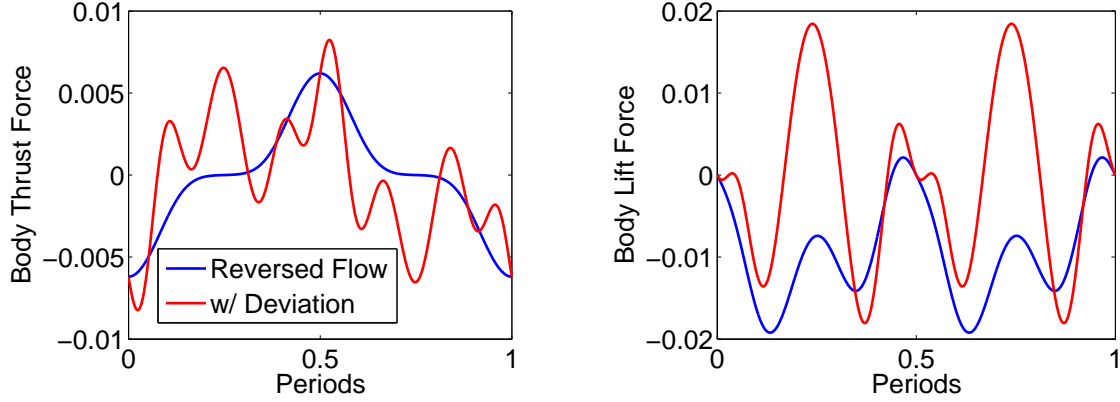

Figure 5.20: Effect of deviation on body forces

5.6.2 Stability of the Time-Varying System

Eigenvalues
-0.01046
-0.004668
0.006717 + 0.009378i
0.006717 - 0.009378i
(a)

Eigenvalues
-0.01038
-0.005489
0.005612 + 0.005475i
0.005612 - 0.005475i
(b)

Eigenvalues
-0.01160
-0.003793
0.006515 + 0.007638i
0.006515 - 0.007638i
(c)

Table 5.16: Eigenvalues for prescribed states: (a) Hover (b) Climb (c) Forward Flight

Comparing the eigenvalues for the case with deviation (Table 5.16) to those of the nominal case (Table 5.10) shows the most similarity of any of the three effects so far explored. The oscillatory modes are unstable for all three conditions in both cases while the static modes are stable. This is clearly visible in the transition from hover to climb and hover to forward flight in Figures 5.21 and 5.22. Comparing these to Figures 5.12 and 5.13 shows similar though not identical magnitudes and trends.
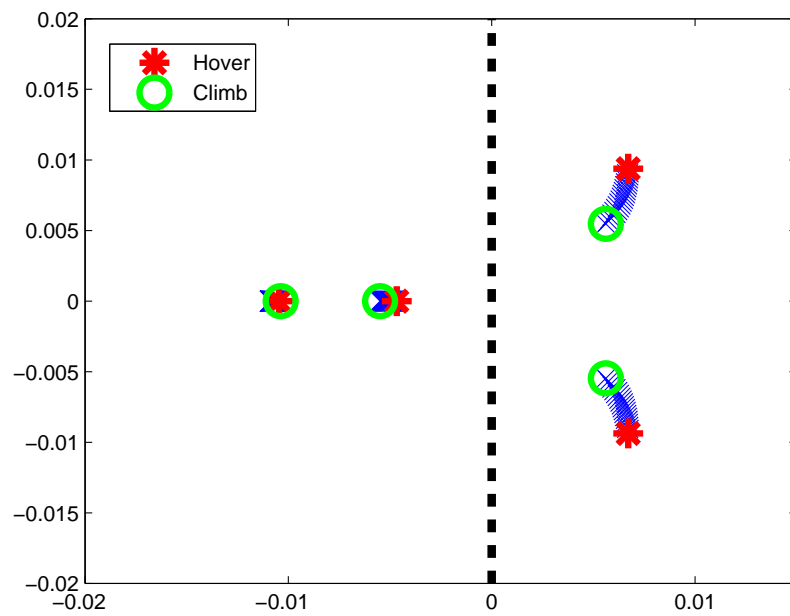
81

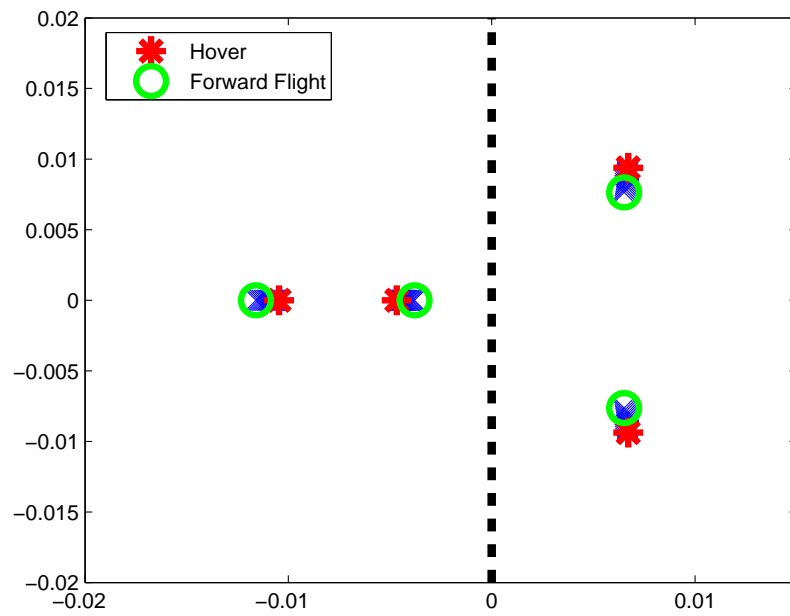Figure 5.21: Root locus plot showing the transition from hover to climb

Figure 5.22: Root locus plot showing the transition from hover to forward flight

5.7   Movement of the Hinge with Respect to the CG

5.7.1   Varying Hinge Location in the Body z Direction

This section alters the system parameters provided in Section 5.1 by varying the hinge location in the body z (vertical) direction from 0 (CG) to 40 mm above the CG.

5.7.1.1   Periodic Trim

Variable	Trim Value	Average
u	0.0005014	7.7938e-11
w	0.01374	7.8008e-06
q	0.2497	-3.4385e-09
Θ	0.04137	-8.7338e-10
κ_0	1.2000e-12	
τ_{max}	1.4301	

(a)

Variable	Trim Value	Average
u	0.0004158	-1.2196e-12
w	0.01501	-6.8662e-06
q	0.4592	3.0978e-09
Θ	0.01387	2.6342e-12
κ_0	2.5644e-13	
τ_{max}	1.4667	

(b)

Variable	Trim Value	Average
u	0.0003320	-2.0541e-10
w	0.01543	-2.5079e-05
q	0.4565	2.2161e-09
Θ	-0.005092	-3.1827e-10
κ_0	-2.6800e-14	
τ_{max}	1.45759	

(c)

Table 5.17: Trim variables for prescribed states while varying the hinge location in the body z direction: (a) 0.04 m (b) -0.01 m (nominal) (c) -0.04

Examining Table 5.17 shows that moving the hinge in the body z direction has very little effect on the trim of the system, only slightly changing the values of any of the trim variables.

5.7.1.2 Stability of the Time-Varying System

Eigenvalues
-0.008175
-0.007534
0.001993 + 0.005386i
0.001993 - 0.005386i
(a)

Eigenvalues
-0.008955
-0.007726
0.003259 + 0.006156i
0.003259 - 0.006156i
(b)

Eigenvalues
-0.008565
-0.007534
0.004450 + 0.006626i
0.004450 - 0.006626i
(c)

Table 5.18: Eigenvalues for prescribed states while varying the hinge location in the body z direction: (a) 0.04 m (b) -0.01 m (nominal) (c) -0.04

Examining Table 5.18 and Figure 5.23 shows very little change in the eigenvalues as the hinge vector changes in the body z direction. One of the static modes (the largest negative magnitude) increases in magnitude until the hinge vector is about -12 mm (the other static mode begins moving to the right before this point). After that point all of the modes move to the right.
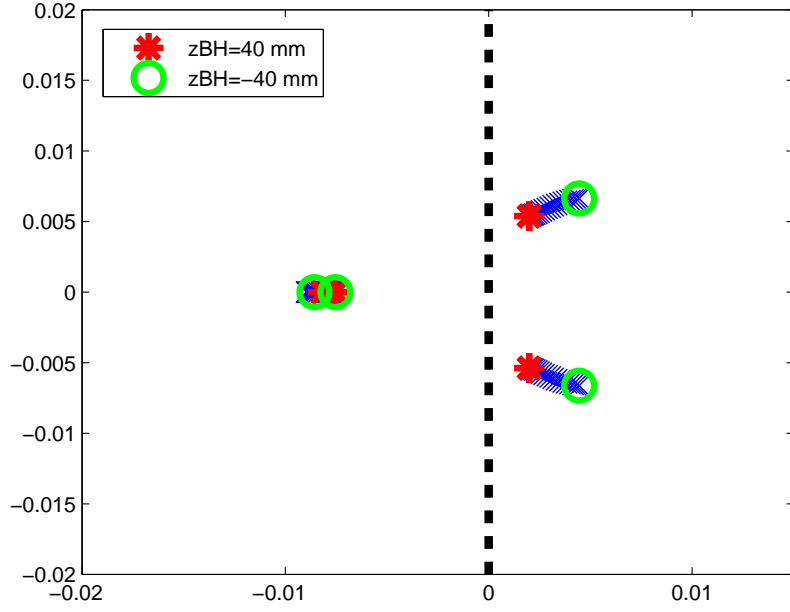
84

Figure 5.23: Root locus plot for varying the hinge location in the body z direction

5.7.2 Varying Hinge Location in the Body x Direction

This section alters the system parameters provided in Section 5.1 by varying the hinge location in the body x (horizontal) direction from - 4 mm to 4 mm above the CG while holding the body z location of the hinge constant at -10 mm.

5.7.2.1 Periodic Trim

Variable	Trim Value	Average
u	0.0004324	1.1464e-05
w	0.01382	-6.8759e-06
q	0.4205	-2.1598e-07
Θ	0.05374	0.0400
κ_0	0.1403	
τ_{max}	1.4671	

(a)

Variable	Trim Value	Average
u	0.0004158	-1.2196e-12
w	0.01501	-6.8662e-06
q	0.4592	3.0978e-09
Θ	0.01387	2.6342e-12
κ_0	2.5644e-13	
τ_{max}	1.4667	

(b)

Variable	Trim Value	Average
u	0.0003537	-1.1464e-005
w	0.01623	-6.8755e-006
q	0.4878	-8.1143e-010
Θ	-0.02231	-0.0400
κ_0	-0.1403	
τ_{max}	1.4671	

(c)

Table 5.19: Trim variables for prescribed states while varying the hinge location in the body x direction: (a) -0.004 m (b) 0 m (nominal) (c) 0.004

Examining Table 5.19 shows that moving the hinge in the body z direction has very little effect on the trim the only large effect being the shift of the average pitch angle and stroke offset to offset the shift in the hinge vector.

5.7.2.2 Stability of the Time-Varying System

Eigenvalues
-0.009157
-0.007457
0.003159 + 0.005989i
0.003159 - 0.005989i

(a)

Eigenvalues
-0.008955
-0.007726
0.003259 + 0.006156i
0.003259 - 0.006156i

(b)

Eigenvalues
-0.009157
-0.007457
0.003159 + 0.005989i
0.003159 - 0.005989i

(c)

Table 5.20: Eigenvalues for prescribed states while varying the hinge location in the body x direction: (a) -0.004 m (b) 0 m (nominal) (c) 0.004

Examining Table 5.20 and Figure 5.24 shows almost no change in the eigenvalues as the hinge vector changes in the body x direction. The largest changes are in the static modes which move towards each other as the hinge moves towards the CG from behind and then back to their original values as the hinge moves forward of the CG. Overall this indicates that the movement of the hinge has little effect on the stability of the system in hover though it would have a larger effect in forward flight modes as this would give the aerodynamic forcing a larger moment arm to act upon the body.
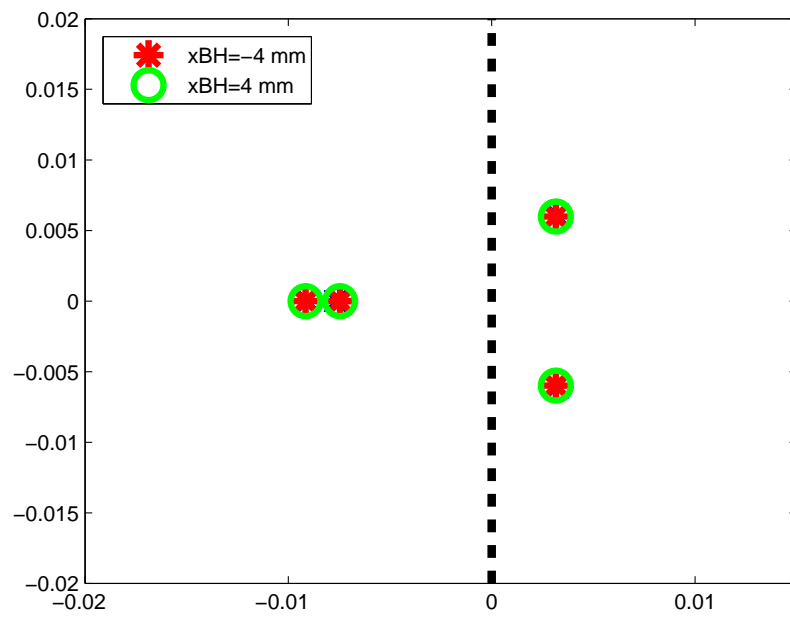
Figure 5.24: Root locus plot for varying the hinge location in the body x direction

Chapter 6

Conclusion and Future Work

In this thesis the influence of various models on the flight dynamics of a flapping wing MAV was investigated. In support of this an aerodynamic model and flight dynamic model were developed in MATLAB and combined into a single simulation model.

The kinetic energy of the system was derived using the quasi-coordinate form of Lagrange's equations with rigid wings and fuselage. The body was assumed to be an ellipsoid while the wings were rectangular and flapped through prescribed kinematics defined by three sinusoidal Euler angles.

The aerodynamic model was based on the Peters airloads model and allowed for the inclusion of unsteady affects through the addition of an inflow model and viscous drag through an empirical model. These models can be easily changed to allow for more complicated wake or viscosity models. The aerodynamic forcing was validated against the quasi-steady aerodynamic model developed by Berman [26], including viscosity as implemented by Stanford [3]. When provided with matching parameters the models were shown to be in good agreement.

For stability analysis a stroke-averaged model and periodic model were used. The stroke-averaged model averaged the forces and mass matrix over one stroke period. The stroke-averaged trim was calculated by the Newton Raphson method until zero-averaged forcing was achieved for prescribed kinematics or flight condition. This was followed by the calculation

of a linearized stability matrix about this trim and from there stability.

The periodic system utilized periodic shooting to find trim, in this case calculating an end state after one period of motion that was equal to the initial condition. The state transition matrix about this trim then provides stability through Floquet analysis. Comparing the stroke-averaged and periodic systems indicates that there are differences that make them not completely interchangeable. A constant inflow model and viscosity model were added to the periodic system so that the stability could be compared to the nominal case (not including either). While the system remained unstable with the addition of the models, it was shown that both have a significant effect on stability (though not necessarily trim) indicating that for this model (and most likely this flight regime) including both of these models is important. Moving the hinge with respect to the center of gravity had little affect on hover stability but with increased physical modeling fidelity such as body drag and introducing a stroke plane angle offset from the body angles the hinge location could have a much larger effect.

For future research, inclusion of more accurate inflow models and viscosity models as well as more complicated physical models would give more accurate comparisons to real world applications. The addition of flexibility to the model as well as a body drag model would also further increase the applicability of the model to a real world simulation. A controller could also be designed to stabilize the system.

Bibliography

[1] Bierling, T., *Nonlinear Dynamics and Stability of Flapping-Wing Flight*, Master's thesis, Technical University of Munich, 2009.

[2] Dickinson, M. H., Lehmann, F.-O., and Sane, S. P., "Wing Rotation and the Aerodynamic Basis of Insect Flight," *Science*, Vol. 284, 1999, pp. 1954–1960.

[3] Stanford, B., Kurdi, M., Beran, P., and McClung, A., "Shape, Structure, and Kinematic Parameterizaon of a Power-Optimal Hovering Wing," *51st AIAA/ASME/ASCE/AHS/ASC Structures, Structural Dynamics, and Materials Conference*, April 2010.

[4] McMichael, J. M. and Francis, M. S., "Micro Air Vehicles - Toward a new Dimension in Flight," Tech. rep., Defence Advanced Research Projects Agency TTO Document, 1996.

[5] "Nano Hummingbird," Website, 2011.

[6] Fry, S. N., Sayaman, R., and Dickinson, M. H., "The Aerodynamics of Free-Flight Maneuvers in Drosophila," *Science*, Vol. 300, April 2003, pp. 495–498.

[7] Fry, S. N., Sayaman, R., and Dickinson, M. H., "The Aerodynamics of Hovering Flight in Drosophila," *The Journal of Experimental Biology*, Vol. 208, 2005, pp. 2303–2318.

[8] Singh, B. and Chopra, I., "Insect-Based Hover-Capable Flapping Wings for Micro Air Vehicles: Experiments and Analysis," *AIAA Journal*, Vol. 46, 2008, pp. 2115–2135.

[9] Zbikowski, R., "On aerodynamic modelling of an insect-like flapping wing in hover for micro air vehicles," *Philosophical Transactions of the Royal Society London A*, Vol. 360, 2009, pp. 273–290.

[10] Nagai, H., Isogai, K., Fujimoto, T., and Hayase, T., "Experimental and Numerical Study of Forward Flight Aerodynamics of Insect Flapping Wing," *AIAA Journal*, Vol. 47, 2009, pp. 730–742.

[11] Dudley, R. and Ellington, C. P., "Mechanics of Forward Flight in Bumblebees, I: Kinematics and Morphology," *Journal of Experimental Biology*, Vol. 148, No. 1, 1990, pp. 19–52.

[12] Isogai, K., Fujishiro, S., Saitoh, T., Yamasaki, M., and Matsubara, M., "Unsteady Three-Dimensional viscous Flow Simulation of Dragonfly Hovering," *AIAA Journal*, Vol. 42, No. 10, 2004, pp. 2053–2058.

[13] Yamamoto, M. and Isogai, K., "Measurement of Unsteady Fluid Dynamic Forces for a Mechanical Dragonfly Model," *AIAA Journal*, Vol. 43, No. 12, 2005, pp. 2475–2480.

[14] Sane, S. P. and Dickinson, M. H., "The aerodynamic effects of wing rotation and a revised quasi-steady model of flapping flight," *The Journal of Experimental Biology*, Vol. 205, 2002, pp. 1087–1096.

[15] Peters, D. A., che A. Hsieh, M., and Torrero, A., "A State-Space Airloads Theory for Flexible Airfoils," *American Helicopter Society 62nd Annual Forum*, American Helicopter Society, Phoenix, AZ, May 2006.

[16] Theodorsen, T., "General Theory of Aerodynamic Instability and the Mechanism of Flutter," Tech. Rep. 496, NACA, May 1934.

[17] Garrick, I. E., "Propulsion of Flapping and Oscillating Airfoil," Tech. Rep. 567, NACA, May 1936.

[18] Loewy, R. G., "A Two-Dimensional Approximation to Unsteady Aerodynamics in Rotary Wings," *Journal of the Aeronautical Sciences*, Vol. 24, No. 2, 1957, pp. 81–92.

[19] Issacs, R., "Airfoil Theory for Flows of Variable Velocity," *Journal of the Aeronautical Sciences*, Vol. 12, No. 1, 1945, pp. 113–117.

[20] Issacs, R., "Airfoil Theory for Rotary Wing Aircraft," *Journal of the Aeronautical Sciences*, Vol. 13, No. 4, 1946, pp. 218–220.

[21] Greenberg, J. M., "Airfoil in Sinusoidal Motion in a Pulsating Stream," Tech. Rep. 1326, NACA, June 1947.

[22] Wagner, H., "Uber die Entstehung des Dynamischen Auftriebs von Tragflugeln," Bd. 5, ZAMM, Feb 1925.

[23] von Karman, T. and Burgers, J. M., *Gerneral Aerodynamic Theory - Perfect Fluids*, Vol. II, Julius Springer, Berlin, 1935.

[24] Pesavento, U. and Wang, Z. J., "Falling Paper: Navier-Stokes Solutions, Model of Fluid Forces, and Center of Mass Elevation," *Physical Review Letters*, Vol. 93, No. 14, 2004, pp. 1–4.

[25] Andersen, A., Pesavento, U., and Wang, Z. J., "Unsteady aerodynamics of fluttering and tumbling plates," *Journal of Fluid Mechanics*, Vol. 541, 2005, pp. 65–90.

[26] Berman, G. J. and Wang, Z. J., "Energy-minimizing kinematics in hovering insect flight," *Journal of Fluid Mechanics*, Vol. 582, 2007, pp. 153–168.

[27] Ellington, C. P., "The Aerodynamics of Hovering Insect Flight. III. Kinematics," *Philosophical Transactions of the Royal Society London B*, Vol. 305, 1984, pp. 41–78.

[28] Oppenheimer, M. W., Doman, D. B., and Sigthorsson, D. O., "Dynamics and Control of a Biomimetic Vehicle Using Biased Wingbeat Forcing Functions: Part I - Aerodynamic Model," *AIAA Aerospace Sciences meeting Including the New Hrozions Forum and Aerospace Exposition*, 2010.

[29] Bierling, T. and Patil, M., "Nonlinear Dynamics and Stability of Flapping-Wing Flight," *International Forum on Aeroelasticity and Structural Dynamics*, 2009.

[30] Sane, S. P. and Dickinson, M. H., "The Control of Flight Force by a Flapping Wing: Lift and Drag Production," *The Journal of Experimental Biology*, Vol. 204, 2001, pp. 2607–2626.

[31] Taylor, G. K., Bomphrey, R. J., and Hoen, J., "Insect Flight Dynamics and Control," *AIAA Aerospace Sciences Meeting and Exhibit*, 2006.

[32] Meirovitch, L. and Tuzcu, I., "Integrated Approach to the Dynamics and Control of Maneuvering Flexible Aircraft," Tech. rep., NASA and Virginia Polytechnic Institute and State University, 2005.

[33] Meirovitch, L., *Methods of Analytical Dynamics*, McGraw-Hill Book Company, New York, 1970.

[34] Deng, X., Schenato, L., Wu, W. C., and Sastry, S. S., "Flapping Flight for Biomimetic Robotic Insects: Part I - System Modeling," *IEEE Transaction on Robotics*, Vol. 22, No. 4, August 2006, pp. 776–788.

[35] Humbert, J. S., Murray, R. M., and Dickinson, M. H., "Pitch-Altitude Control and Terrain Following Based on Bio-Inspired Visuomotor Convergence," *AIAA Guidance, Navigation, and Control Conference and Exhibit*, 2005.

[36] Faruque, I. and Humbert, J. S., "Dipteran insect flight dynamics. Part 1 Longitudinal motion about hover," *Journal of Theoretical Biology*, Vol. 264, May 2010, pp. 538–552.

[37] Faruque, I. and Humbert, J. S., "Dipteran insect flight dynamics. Part 2: Lateral-directional motion about hover," *Journal of Theoretical Biology*, Vol. 265, May 2010, pp. 206–313.

[38] Sun, M. and Xiong, Y., "Dynamic flight stability of a hovering bumblebee," *The Journal of Experimental Biology*, Vol. 208, 2005, pp. 447–459.

[39] Hamel, P. G. and Jategaonkar, R. V., "Evolution of Flight Vehicle System Identification," *Journal of Aircraft*, Vol. 33, 1996, pp. 9–28.

[40] Hedrick, T. L., Cheng, B., and Deng, X., "Wingbeat Time and the Scaling of Passive Rotational Damping in Flapping Flight," *Science*, Vol. 324, 2009, pp. 252–255.

[41] Doman, D. B., Oppenheimer, M. W., and Sightorsson, D. O., "Wingbeat Shape Modulation for Flapping Wing Micro Air Vehicle Control During Hover," *Journal of Guidance, Control, and Dynamics*, Vol. 33, No. 3, May-June 2010, pp. 724–739.

[42] Liu, H., Nakata, T., Gao, N., Maeda, M., Aono, H., and Shyy, W., "Micro air vehicle-motivated computational biomechanics in bio flights: aerodynamics, flight dynamics and maneuvering stability," *Acta Mechanica Sinica*, Vol. 26, No. 6, December 2010, pp. 863–879.

[43] Deng, X., Schenato, L., and Sastry, S. S., "Flapping Flight for Biomimetic Robotic Insects: Part II - Flight Control Design," *IEEE Transaction on Robotics*, Vol. 22, No. 4, August 2006, pp. 789–803.

[44] Oppenheimer, M. W., Doman, D. B., and Sightorsson, D. O., "Dynamics and Control of a Minimally Actuated Biomimetic Vehicle: Part II - Control," *AIAA Guidance, Navigation, and Control Conference*, 2009.

[45] Stevens, B. L. and Lewis, F. L., *Aircraft Control and Simulation*, John Wiley and Sons, Hoboken, NJ, 2003.

[46] Moore, J., Stanford, B., McClung, A., and Beran, P., "Variable-Fidelity Kinematic Optimization of a Two-Dimensional Hovering Wing," *49th AIAA Aerospace Sciences Meeting including the New Horizions Forum and Aerospace Exposition*, AIAA, January 2011.

[47] Johnson, W., *Helicopter Theory*, Princeton University Press, 1980.

[48] Ellington, C. P., "The Aerodynamics of Hoverying Insect Flight. II. Morphological Parameters," *Philosophical Transactions of the Royal Society London B*, Vol. 305, 1984, pp. 17–40.

[49] Hedrick, T. L. and Daniel, T. L., "Flight control in the hawkmoth Manduca sexta: the inverse problem of hovering," *The Journal of Experimental Biology*, Vol. 209, 2006, pp. 3114–3130.

[50] Willmott, A. P. and Ellington, C. P., "The Mechanics of Flight in the Hawkmoth Manduca Sexta. I. Kinematics of Hovering and Forward Flight," *The Journal of Experimental Biology*, Vol. 200, 1997, pp. 2705–2722.

[51] Richter, M. and Patil, M., "Influence of Wing Flexibility on the Stability of Flapping Flight," *AIAA Atmospheric Flight Mechanics Conference*, 2010.